Three-dimensional feedback processes in current-driven metal

E. P. Yu,[1,*] T. J. Awe,[1] K. R. Cochrane,[1] K. J. Peterson,[1] K. C. Yates,[1,2] T. M. Hutchinson ,[3] M. W. Hatch,[4]
B. S. Bauer,[5] K. Tomlinson,[6] and D. B. Sinars [1]

[1]*Sandia National Laboratories, Albuquerque, New Mexico 87185, USA*
[2]*Los Alamos National Laboratory, Los Alamos, New Mexico 87545, USA*
[3]*Lawrence Livermore National Laboratory, Livermore, California 94550, USA*
[4]*Department of Electrical and Computer Engineering, University of New Mexico, Albuquerque, New Mexico 87131, USA*
[5]*Department of Physics, University of Nevada, Reno, Reno, Nevada 89506, USA*
[6]*General Atomics, San Diego, California 92121, USA*

Using three-dimensional (3D) magnetohydrodynamic simulations, we study how a pit on a metal surface evolves when driven by intense electrical current density **j**. Redistribution of **j** around the pit initiates a feedback loop: **j** both reacts to and alters the electrical conductivity σ, through Joule heating and hydrodynamic expansion, so that **j** and σ are constantly in flux. Thus, the pit transforms into larger striation and filament structures predicted by the electrothermal instability theory. Both structures are important in applications of current-driven metal: The striation constitutes a density perturbation that can seed the magneto-Rayleigh-Taylor instability, while the filament provides a more rapid path to plasma formation, through 3D **j** redistribution. Simulations predict distinctive self-emission patterns, thus allowing for experimental observation and comparison.

I. INTRODUCTION

Metals commonly contain an abundance of defects, including μm-scale resistive inclusions [1,2] and voids [3]. These obstacles force electrical current density **j** to deflect and, as a consequence, develop regions of enhanced **j**. While the small size of defects suggests a correspondingly small **j** amplification, in fact theory and simulation show this is not the case. From the analogy between hydrodynamic and electrical current flow [4,5], we can understand flow of **j** around resistive obstacles through the corresponding solutions for ideal, incompressible hydrodynamic flow, which obey the similarity principle (e.g., Ref. [6]). Consequently, assuming for instance a spherical void, **j** amplifies at the equator by a factor of 3/2 above its unperturbed value, *independent* of void diameter, which only determines the characteristic scale length of the flow pattern.

Non-negligible **j** amplification driven by defects results in a corresponding increase in Joule heating j^2/σ, where σ is the electrical conductivity. Due to the dependence of σ on temperature T in metals (i.e., $d\sigma/dT < 0$ as seen in Fig. 1), Joule heating can trigger a feedback loop: Regions of higher j and j^2/σ will drive higher T and lower σ, which causes **j** to redistribute out of this region and amplify elsewhere. Consequently, as the peak in j shifts, so does the peak in Joule heating. This effect is well studied in one dimension (1D) in nonlinear magnetic diffusion (NLMD) propagation [8–13]: When electrical current is applied to a metal, **j** must gradually diffuse into the metal from the surface, occupying a resistive skin depth δ. Due to Joule heating, σ falls in the outermost, hotter, current-carrying layer δ, causing the peak in j and j^2/σ to redistribute inward to cooler, higher-σ metal, which then overheats. Hence, the region of hotter, lower-σ metal near the surface continuously grows, while the peak in j and j^2/σ continuously burrows deeper into the metal.

Let r denote the characteristic dimension of the conductor cross section; for instance, in a cylindrical rod with **j** flowing along the axis, r corresponds to the rod radius. In a "thick" conductor satisfying $r \gg \delta$ (which is the case of interest in this work), NLMD effects become important when j is sufficiently intense as to lower σ to roughly half its room temperature value. More conveniently, this condition can be recast as a minimum magnetic field strength $B > B_m$ (e.g., $B_m \sim 31$ T for aluminum [8,10]).

While the above 1D description is suitable for a perfectly homogeneous metal, more realistically we must superpose the NLMD picture on top of localized enhanced Joule heating driven by 3D defects. The region of enhanced Joule heating is of similar size to the defect, so for μm-scale defects we might expect the overheated regions to play a minor role in applications of much larger size. However, just as feedback allowed the resistive region δ to grow in NLMD (through the shifting Joule heating peaks), so might feedback allow isolated defects to grow and transform.

Structures towards which 3D defects might evolve were anticipated decades ago, in the context of the Joule heating-driven electrothermal instability (ETI) [14–21]. Consider current flowing vertically through a metal that is thin relative to δ, so that **j** is fully diffused. Assuming 2D plane wave solutions (see Appendix A for a brief overview of linear ETI theory), ETI predicts that in solid or liquid metals,
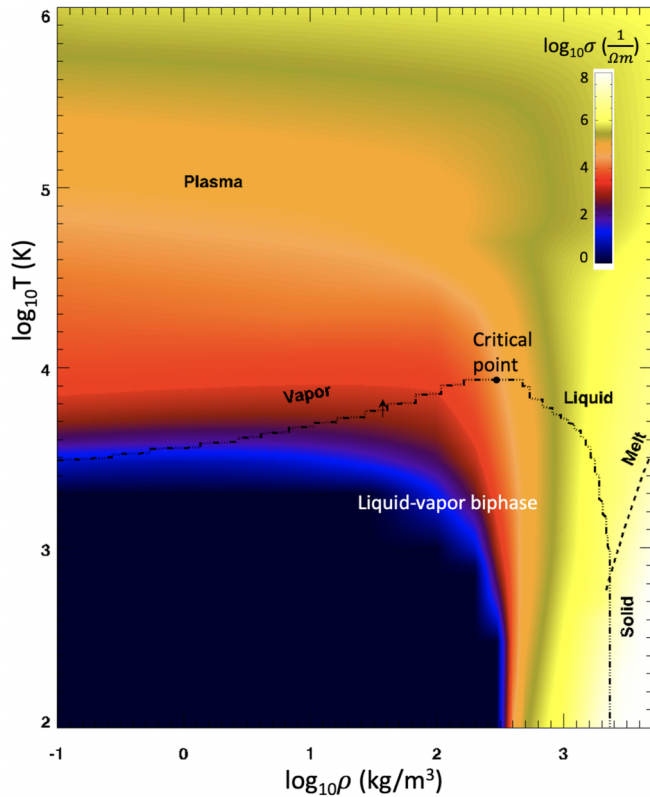
*epyu@sandia.gov

FIG. 1. Electrical conductivity σ $(1/\Omega m)$ of aluminum from the Lee-More-Desjarlais model [7], overlaid on a phase diagram showing solid, liquid, liquid-vapor biphase, and vapor boundaries. In the solid and liquid phases, $d\sigma/dT < 0$, while in the liquid-vapor and vapor phases, $d\sigma/dT > 0$.

where $d\sigma/dT < 0$ (see Fig. 1), horizontally oriented, overheated, lower-density "striations" will develop. Striations are important in applications using magnetically accelerated metal, including magnetoinertial fusion [22–31]. Here $\mathbf{j}$ is driven through cylindrical metal shells (also known as liners) that then implode due to the interaction of the self-generated magnetic field $\mathbf{B}$ with current (i.e., $\mathbf{j} \times \mathbf{B}$ force). Density perturbations on the liner surface will be amplified by the magneto-Rayleigh-Taylor instability (e.g., Refs. [15,32–35]), resulting in large-scale perturbations [36] that can degrade performance. Because the magneto-Rayleigh-Taylor instability acts most virulently on perturbations aligned perpendicular to $\mathbf{j}$, the striation constitutes an ideal seed.

Once the Joule-heated metal expands into the vapor phase where $d\sigma/dT > 0$, the dominant ETI mode rotates from horizontal striations to overheated vertical "filaments." Filaments are important in understanding how and when plasma initiates on the metal surface, which is another design consideration in current-driven metal applications. In magnetoinertial fusion, plasma formation on the outer liner surface can shunt current away from the liner [37] and develop magnetohydrodynamic (MHD) instabilities, reducing performance. The inner liner surface bounds fusion fuel, and plasma formation here [38] can mix liner material into the fuel, reducing fusion yield. Experiments studying plasma formation on Joule-heated metal show overheated structures aligned parallel to $\mathbf{j}$ [1,20,39,40], suggesting ETI filament development.

While both striations and filaments have been predicted in 2D ETI theory, basic questions remain: How do striations develop from isolated 3D defects? How do horizontal striations transform into vertical filaments? Given the orthogonal orientation of these modes, we expect this is a 3D process, possibly driven by the aforementioned feedback loop acting on a 3D perturbation.

In order to trigger the feedback loop, we consider a *nonlinear* perturbation, which drives a current perturbation $\delta\mathbf{j}$ on order the equilibrium current $\mathbf{j_0}$. In this case, the resulting δT (due to enhanced Joule heating) and $\delta\sigma$ will also be comparable to the equilibrium T_0 and σ_0, thus altering the equilibrium and initiating the feedback loop. Considering a void perturbation, the magnitude of δj is independent of void size but depends on its shape. For instance, a skinny, pen-shaped ellipsoid (with major axis aligned along $\mathbf{j_0}$) generates $\delta j \ll j_0$ [4,41] and is thus a linear perturbation, whereas a spherical void is a nonlinear perturbation, resulting in $\delta j / j_0 = 1/2$.

In this work, we use MHD simulations to show how a 3D nonlinear perturbation (i.e., a hemispherical pit on the metal surface) self-consistently seeds both the striation and filament forms of ETI through the feedback loop connecting $\mathbf{j}$ and σ. The striation is a hot strip aligned transverse to $\mathbf{j}$, which, owing to its lower density ρ, serves as a seed to later magneto-Rayleigh-Taylor growth. The filament is aligned parallel to $\mathbf{j}$ and coexists simultaneously with the striation but at larger radius in the lower-ρ vapor. The filament illustrates the 3D nature of plasma formation, achieving plasmalike temperatures significantly earlier than an equivalent 1D simulation, owing to ETI-enhanced Joule heating.

Simulations predict that nonuniform heating seeded by the pit results in distinctive, evolving self-emission patterns, and in fact recent experiments [42] have validated these predictions. While qualitative and quantitative discrepancies exist between simulation and experiment, the overall good agreement is vital to the credibility of the simulations. The experimental paper [42] also briefly describes simulation results, to the extent necessary to understand the origin of the emission patterns, but does not address the striation development or details of filament formation; we reserve this discussion for the present paper, as well as the companion paper [43].

Metals driven by intense electrical current are used in a range of applications including laboratory astrophysics [44,45], material property studies [37,46–49], magnetic flux compression [8,10,50], and magnetoinertial fusion. Accordingly, the work in this paper is most relevant to high-energy-density applications [51,52]. However, it may also inform other areas of physics. For instance, the ETI filament is closely connected to the "short circuit" instability [53–55], proposed as a heating mechanism in meteorites. Furthermore, the growth of the pit, due to Joule heating, into the larger ETI striation bears a resemblance to the "quench" process in superconductors [56,57], where a region of enhanced Joule heating (due to surface defects) [58,59] exceeds the critical temperature at which superconductivity is lost, and this region of lower σ quickly spreads [60]. In laser-driven inertial confinement fusion, the growth of isolated defects (through hydrodynamic instabilities) and their impact on performance is also actively studied (e.g., Refs. [61–66]). Finally, switching to more of an engineering perspective, the structural damage
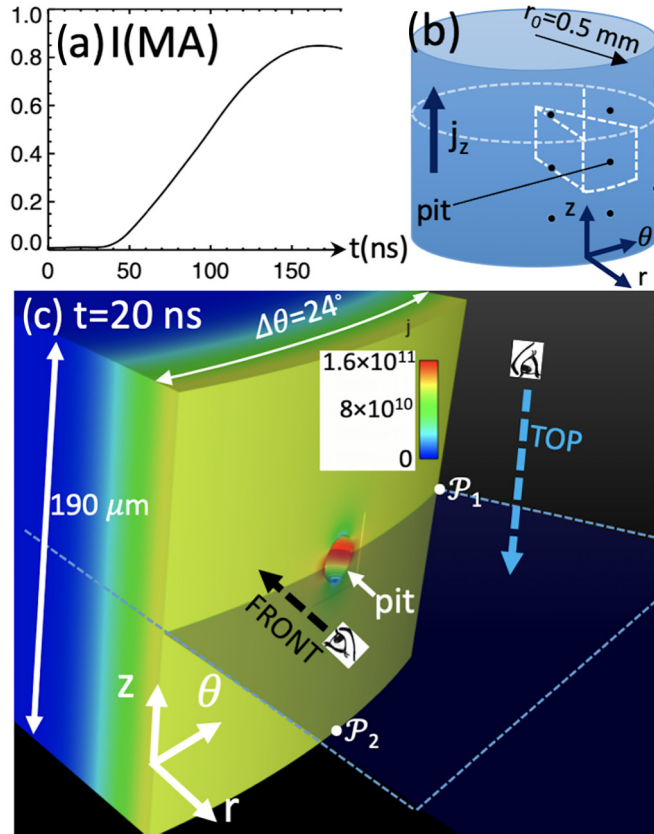
FIG. 2. Computational setup. (a) Current drive applied to rod. (b) Simulation scenario: aluminum rod of radius r_0, with evenly spaced hemispherical pits removed from the surface (only 9 are shown). (c) Periodic wedge with a single pit, colored by j (A/m^2). Also shown are front or top visualization planes; subsequent top views show the midplane $z_m = 95$ μm, unless otherwise noted. $\mathcal{P}_1$ and $\mathcal{P}_2$ represent points at the azimuthal and axial boundaries of the wedge, respectively, used in the text to estimate the importance of interpit communication through the periodic boundary conditions.

caused by electromagnetically driven defect growth has been studied in lower-$\mathbf{j}$, nonimploding systems such as magnetic confinement fusion (i.e., crack development in tokamak walls [67]), microelectronic circuit lines, and metallic structures exposed to lightning strikes [68,69].

The paper is organized as follows: Section II introduces 3D MHD simulations of a current-driven metal rod with a periodic array of pits on the surface. Section III describes the transformation of a pit into a bump due to the feedback process, and the ensuing formation of the striation as well as hot spots. Section IV shows how the hot spot explosion results in expanding plumes in which the plasma filament develops. Comparison with 1D simulation illustrates how the different trajectory in equation-of-state space followed in 3D (due to the ETI instability) allows earlier plasma formation. We conclude in Sec. V.

II. 3D MHD SIMULATION

We use the MHD code Alegra [70] to model experiments applying a $\sim$0.85 MA current pulse $I(t)$ [Fig. 2(a)] to a 1-mm-diameter aluminum (Al) rod, on the surface of

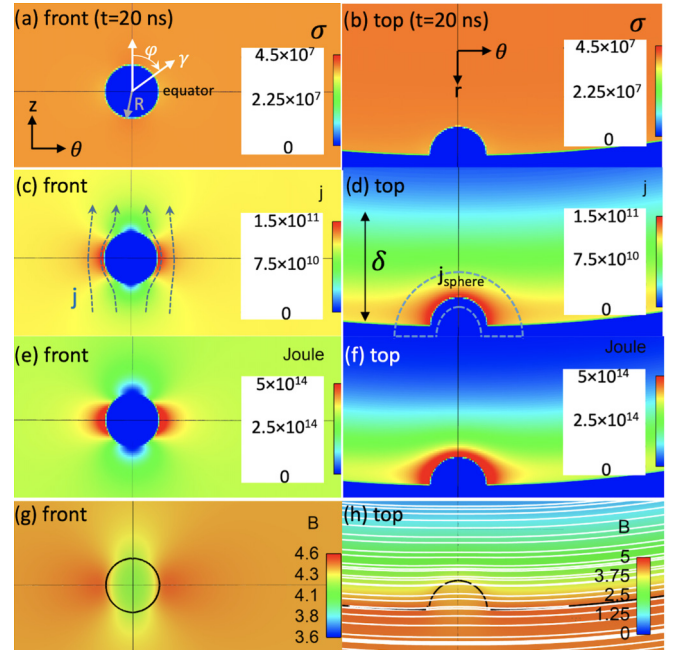FIG. 3. Flow around a hemispherical pit $\mathbf{j}_{\text{sphere}}$, at $t = 20$ ns. Panels (a), (c), (e), and (g) visualize the surface of the rod ($r = 0.5$ mm), showing σ (1/Ωm), j (A/m^2) with representative $\mathbf{j}$ streamlines, j^2/σ (W/m^3), and B (T). Panels (b), (d), (f), and (h) show the corresponding top views. In (g) and (h), the pit boundary is represented by the the black circle and semicircle, respectively. In (h) the white lines represent magnetic field streamlines (the tangent to a streamline gives the direction of $\mathbf{B}$).

which we machine 20-μm-diameter hemispherical pits [42]. A SESAME equation of state [71] models the rod, which is initialized at room temperature $T = 294$ K (all units are SI). To capture the relation between stress and strain [18,72], we include material strength (elastic-plastic constitutive model combined with the Steinberg-Guinan-Lund yield model). Electrical and thermal conductivities are provided by the Lee-More-Desjarlais model [7]. The aforementioned material models, in conjunction with Alegra, have been validated by > 15 years of dynamic materials research at Sandia National Laboratories (e.g., Refs. [46,48]).

Simulations assume ion and electron temperatures are equal and do not account for radiative losses; estimates show these assumptions are valid for the densities and temperatures considered in this paper. To keep the (Eulerian) computational domain tractable, we only model a section of the rod, using the wedge geometry shown in Figs. 2(b) and 2(c), with periodic boundary conditions in both the axial (i.e., z) and azimuthal (i.e., θ) directions. At the outermost boundary $r_{\text{max}} = 0.8$ mm, we apply the boundary condition $\mathbf{B} = \frac{\mu_0 I(t)}{2\pi r_{\text{max}}}\hat{\theta}$, which physically corresponds to a perfectly conducting boundary at r_{max}. To resolve $\mathbf{j}$ redistribution around the pit, we use fine resolution (0.5 μm) in its vicinity.

Figure 3 visualizes the outer surface of the rod $r_0 = 0.5$ mm at early time, when the rod is near room temperature, so that σ is uniform aside from the pit [see Figs. 3(a) and 3(b)]. As described in Ref. [5], the flow of $\mathbf{j}$ around the pit can be understood in terms of its analogous ideal hydrodynamic flow velocity. For the case of a pit of radius R embedded in a

uniform flow $j_0 \hat{z}$, the solution is

$$\mathbf{j}_{\text{sphere}} = j_0 \cos\phi\left(1 - \frac{R^3}{\gamma^3}\right)\hat{\gamma} - j_0 \sin\phi\left(1 + \frac{R^3}{2\gamma^3}\right)\hat{\phi}, \quad (1)$$

where radial coordinate γ and angular coordinate ϕ are defined in Fig. 3(a). The first term in each parentheses corresponds to the uniform flow $j_0 \hat{z}$, while the second term captures the modification in flow due to the pit, which decays rapidly as R^3/γ^3. Just as in hydrodynamic flow around an impenetrable sphere, $\mathbf{j}$ deflects around the pit [Fig. 3(c)], resulting in reduced j at the poles $\phi = 0, \pi$ (i.e., stagnation points in the analogous hydrodynamic flow), and amplified j around the equator $\phi = \pi/2$, which in turn leads to enhanced j^2/σ there [Figs. 3(e) and 3(f)]. Maximum j amplification is reached at the edge of the pit ($\gamma = R$, $\phi = \pi/2$), where $\mathbf{j}_{\text{sphere}} = \frac{3}{2}j_0 \hat{z}$. Hence, j amplifies by a factor 3/2, independent of pit size R.

The top view [Fig. 3(d)] shows that j consists of j_{sphere} in addition to the magnetic diffusion solution. To elaborate, in the absence of the pit, j will diffuse radially inward from the rod surface, occupying a constantly growing resistive skin depth δ, illustrated in Fig. 3(d); this behavior is described by the 1D (radial) magnetic diffusion solution. In our problem of interest, the magnetic diffusion solution is superposed on top of j redistribution due to the pit j_{sphere}, corresponding to enhanced j within the blue contour. We should also consider the contribution to $\mathbf{j}$ from adjacent pits, due to periodic boundary conditions in Fig. 2(b). However, if the periodic wedge is sufficiently large relative to R, then the influence of adjacent pits is negligible. We can estimate this effect by evaluating $\mathbf{j}_{\text{sphere}}$ at the wedge boundaries; if $\mathbf{j}_{\text{sphere}}$ is approximately the unperturbed value $j_0 \hat{z}$, then the modification to $\mathbf{j}$ due to the pit has decayed sufficiently that we can regard pits as noninteracting. In fact, this is the case for the wedge shown in Fig. 2(c): at the azimuthal boundary (see point $\mathcal{P}_1$, located at $\gamma = 104.7$ μm, $\phi = \pi/2$), $\mathbf{j}_{\text{sphere}} = 1.0004 j_0 \hat{z}$, and at the axial boundary (see point $\mathcal{P}_2$, located at $\gamma = 95$ μm, $\phi = \pi$), $\mathbf{j}_{\text{sphere}} = 0.9988 j_0 \hat{z}$.

As seen in Fig. 3(g), vanishing $\mathbf{j}$ in the pit results in a modest magnetic field decrease $\delta B/B_0 \sim 5\%$, where $B_0 = \frac{\mu_0 I}{2\pi r_0}$ is the value of B at the rod surface $r = r_0$ in the absence of the pit. Note that Fig. 3(g) focuses on a narrow range of B to emphasize δB. The top view of B in Fig. 3(h) includes $\mathbf{B}$ streamlines which point nearly azimuthally, as would be the case for a perfectly smooth rod. At very early time (e.g., $t = 1$ ns), the current skin depth δ is so small that the metal approximates a perfect conductor, with the associated boundary condition $\mathbf{B} \cdot \mathbf{n} = 0$ ($\mathbf{n}$ is a vector normal to the rod surface). In this case, $\mathbf{B}$ does not point purely azimuthally, rather dipping into the pit so as to conform to the metal surface. However, as $\mathbf{j}$ continues to diffuse deeper into the metal, the $\mathbf{B} \cdot \mathbf{n} = 0$ condition relaxes, so that $\mathbf{B}$ pierces the surface. Such is the case shown in Fig. 3(h), although we can still see evidence of $B_r \neq 0$, as $\mathbf{B}$ dips slightly into the pit.

Later in time, the Joule heating pattern in Figs. 3(e) and 3(f) results in higher T, as seen in Figs. 4(a) and 4(b). As estimated in the Supplemental Material to Ref. [43], thermal conduction losses are negligible compared to Joule heating for $R = 10$ μm

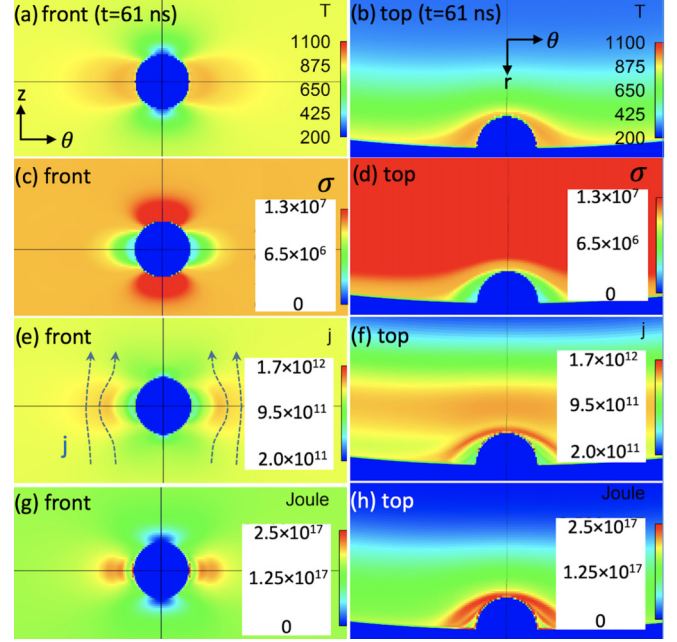FIG. 4. Melt propagation due to $\mathbf{j}$ redistribution, at $t = 61$ ns. Front views visualize $r = 0.5$ mm. The hottest region closest to the pit, visualized in (a) and (b), has melted, reducing σ there and forcing $\mathbf{j}$ to redistribute further from the pit. Units are T (K), σ (1/Ωm), j (A/m²), and j^2/σ (W/m³).

pits, during this phase of pit evolution. Once the overheated region around the pit equator begins the melt transition, σ drops by $\sim 3\times$ [Figs. 4(c) and 4(d)], thus initiating the 3D feedback loop intertwining $\mathbf{j}$ and σ. As seen in Figs. 4(e) and 4(f), $\mathbf{j}$ diverts around the melting region, so that $\mathbf{j}$ and j^2/σ [Figs. 4(g) and 4(h)] peak further from the pit. Consequently this region overheats until it also melts. In this way, $\mathbf{j}$ continuously shifts further from the pit, so as to grow the hotter, melted region in the radial and azimuthal directions. This process, which has been described in Refs. [18,73], continues so long as the sharp σ contrast between melted and unmelted metal exists.

III. STRIATION DEVELOPMENT

At $t = 69$ ns, with the exception of the cooler, high-σ stagnation points at the poles of the pit, the entire surface has melted [Fig. 5(c)], thus quenching the drive mechanism responsible for melt propagation in Fig. 4. At this time, the pit is again the dominant σ perturbation, causing $\mathbf{j}$ to deflect around the pit and amplify around the equator [Figs. 5(e) and 5(f)], similarly to $\mathbf{j}_{\text{sphere}}$ in Fig. 3. Because the rod surface has melted, material strength vanishes and hydrodynamic expansion begins in earnest, further altering the σ topography by deforming the rod surface. We note that in an equivalent 1D radially resolved simulation, $\Delta r = 0.5$ μm resolution (used also in 3D simulation) shows close agreement with experimental expansion rates [74].

The overheated region around the pit [Figs. 5(a) and 5(b)] is hottest and expands first. As shown in Fig. 5(b), the void creates a pressure gradient which azimuthally *focuses* the resulting expansion, similarly to the "shaped-charge" effect
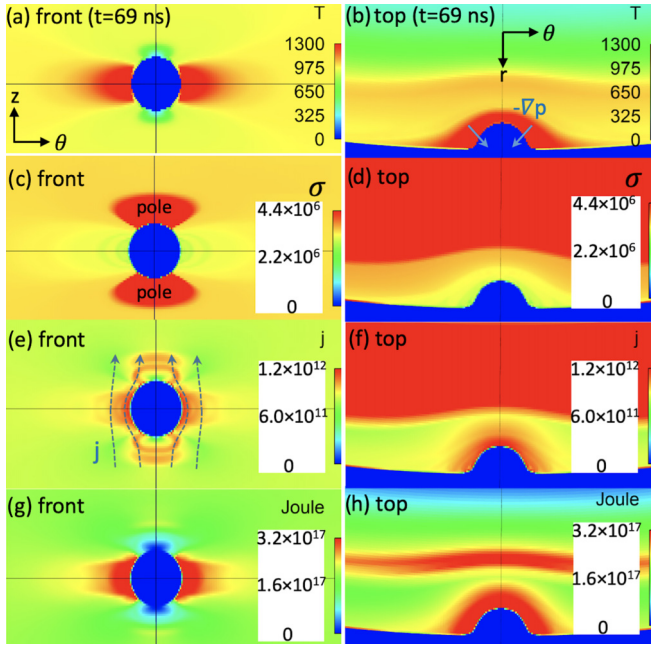
FIG. 5. Postmelt **j** at $t = 69$ ns. Front views visualize $r = 0.5$ mm. Except for the poles, the rod surface has melted, quenching the σ contrast responsible for the melt propagation process seen in Fig. 4. Units are identical to Fig. 4.

FIG. 6. By $t = 80$ ns, expansion transforms the pit into a bump, qualitatively changing the **j** flow pattern from $\mathbf{j}_{sphere}$ to $\mathbf{j}_{bump}$. (a) Rod surface illustrating the bump (white dotted semicircle). The side viewing plane cuts through the center of the bump at $\theta = 0°$. [(b) and (c)] Front view of j (A/m^2) and j^2/σ (W/m^3) near the rod surface ($r = 0.499$ mm) with representative **j** streamlines. (d) Top view of density ρ (kg/m^3). (e) Side view, showing j peaking at the base of the bump.

[75,76]. Hence, as overheated metal surrounding the pit expands, it concentrates into the center of the pit, forming a bump by $t = 80$ ns [Figs. 6(a) and 6(d)], while also resulting in a region of lower density ρ behind the bump [bounded by the gray curve in Fig. 6(d)]. Due to bump formation, **j** no longer deflects *around* a pit (i.e., azimuthally away and radially inward) but rather flows *into* the bump (i.e., azimuthally toward and radially outward), as illustrated by **j** streamlines in Figs. 6(b) and 6(e). In the 2D (r, z) solution for hydrodynamic flow over a bump (see Appendix B), flow is fastest at the base of the bump, where the surface transitions from curved to flat. Similarly, in our electrical problem, $\mathbf{j}_{bump}$ peaks at the bump base [Figs. 6(b) and 6(e)], leading to peaks in j^2/σ there [Fig. 6(c)]. This flow pattern contrasts with the original $\mathbf{j}_{sphere}$ solution, seen in Fig. 3.

To determine the timescale on which the $\mathbf{j}_{sphere}$ solution switches to $\mathbf{j}_{bump}$, we recall the magnetic field evolution equation:

$$\frac{\partial \mathbf{B}}{\partial t} = \nabla \times (\mathbf{v} \times \mathbf{B}) + \frac{1}{\mu_0 \sigma} \nabla^2 \mathbf{B}. \qquad (2)$$

The first term on the right-hand side is dominant in a perfect conductor and describes how **B** is "frozen" into a medium moving with velocity **v**; the second term describes resistive diffusion of **B** into a medium with finite σ. The relative importance of terms, found through simple dimensional considerations, is quantified through the magnetic Reynolds number $R_M \sim \mu_0 \sigma v l$, where l is a typical length scale, in this case representative of the pit or bump size. Using $\sigma \sim 2 \times 10^6$ $1/\Omega$m, $v \sim 1500$ m/s, and $l \sim 10$ μm, we estimate $R_M \sim 0.04$, so the resistive diffusion term is dominant. In this case, once again dimensional arguments yield the timescale
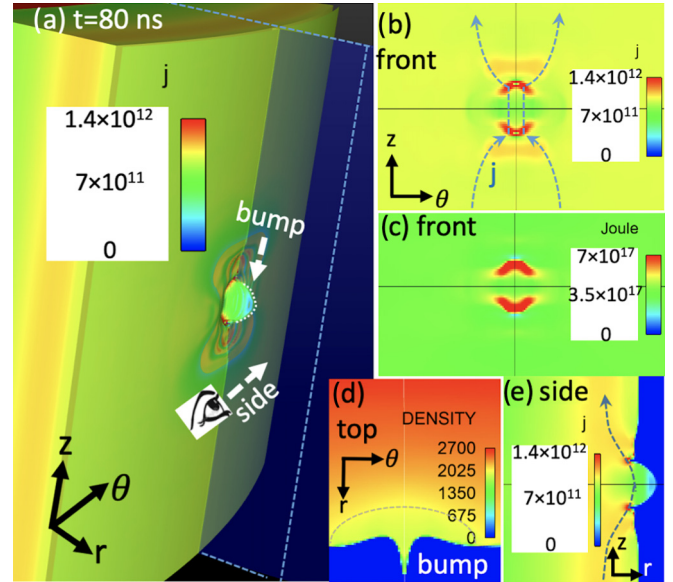
on which **B** and **j** respond (via diffusion) to the evolving conductivity: $\tau_R \sim \mu_0 \sigma l^2 \sim 0.25$ ns. Because this timescale is so much faster than the hydrodynamic timescale $\tau_H \sim 10$ ns on which the pit transforms into a bump, **j** can effectively respond instantaneously to changes in σ during this process.

Later in time, the bump-driven Joule heating pattern shown in Fig. 6(c) persists at the rod surface [Fig. 7(a)] and drives two hot spots (HS), visualized in Fig. 7(b). A simulated self-emission image is generated using the postprocessing code SPECT3D [77], which solves the radiative transfer equation along lines-of-sight through the computational grid. At each volume element along the line-of-sight, the frequency-dependent absorption and emissivity of aluminum are computed, under the assumption of local thermodynamic equilibrium. Photon energies in the visible range (1.65–3.26 eV) are used in computing Fig. 7(c), which shows the HS and allows comparison to experiments [42], which in fact have validated the simulation prediction.

Figure 7(c) does not resolve another overheated structure that lies too deep within the metal to be visible in self-emission. This structure—a nascent ETI striation—is visualized in Fig. 7(d). The striation, roughly bounded by the $\sigma = 7.5 \times 10^5$ $1/\Omega$m contour, is broader than the HS in Fig. 7(b), as well as lower ρ than surrounding metal [Fig. 7(e)]. Its origin traces back to the overheated metal surrounding the pit in Figs. 5(a) and 5(b), which expands, creating the hotter, lower-ρ region bounded by the gray curve in Fig. 6(d). In relation to Fig. 1, the striation sits in the melted metal phase, where $d\sigma/dT < 0$ and $d\sigma/d\rho > 0$. Consequently, the lower ρ and higher T in the striation results in lower σ there [i.e., using a subscripted S to denote the
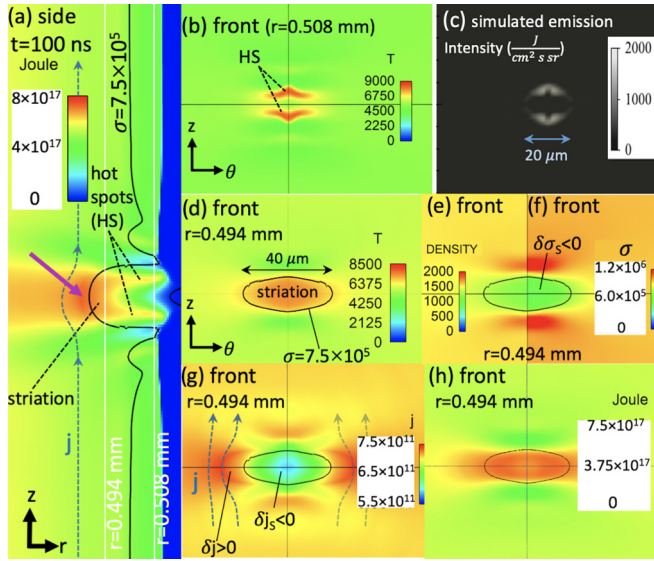
FIG. 7. At $t = 100$ ns, the Joule heating pattern arising from j_{bump} results in hot spots (HS) near the rod surface, as well as a striation deeper in the metal. (a) Side view of j^2/σ. White vertical lines show $r = 0.494$ and 0.508 mm, while the solid black line represents the $\sigma = 7.5 \times 10^5$ $1/\Omega$m contour. (b) HS near rod surface should be visible in (c) visible self-emission. The striation, observed in (d)–(h), has lower electrical conductivity σ relative to surrounding metal, forcing **j** to divert around and amplify at the edges. The resulting enhanced j^2/σ drives striation growth in the azimuthal and radial directions. Units are j^2/σ (W/m³), T (K), ρ (kg/m³), σ (1/Ωm), and j (A/m²).

striation, $\delta\sigma_S < 0$ in Fig. 7(f)] and, consequently, lower j [$\delta j_S < 0$ in Fig. 7(g)]. Nevertheless, the striation experiences enhanced j^2/σ [Fig. 7(h)] and thus continues to overheat, because the enhancement in j^2/σ due to $\delta\sigma_S < 0$ overcomes the reduction due to $\delta j_S < 0$. As shown in Appendix A, a similar scenario occurs even in 2D, when the striation is oriented at an angle to the current flow (i.e., $\pi/4 < \alpha < \pi/2$ in Appendix A).

Note that $\delta\sigma_S < 0$ causes **j** to divert azimuthally around the striation, as shown in Fig. 7(g), so j and j^2/σ amplify at the edges, similarly to flow around the pit. In this way, the striation continuously widens by converting high-σ, dense metal at the edges into hotter, expanded, lower-σ metal, characteristic of the striation. The **j** redistribution responsible for striation widening also applies in the radial direction: As seen in Fig. 7(a), the striation constitutes a low-σ "divot" which forces **j** to divert inward and amplify at the divot tip (see Appendix B). Consequently a local peak in j^2/σ develops there [see the magenta arrow in Fig. 7(a)], and the resulting overheating allows the striation to propagate deeper into the metal. Similar behavior has been observed computationally and experimentally in the study of crack growth in electrical conductors [68,69].

IV. CRATER AND PLASMA FILAMENT FORMATION

At $t = 115$ ns, the striation has continued to heat and widen through the mechanisms described above. Closer to the rod surface, the overheated HS in Figs. 7(a) and 7(b) explode,

creating expanding plumes as well as craters, as seen in Figs. 8(a) and 8(b). The $\rho = 400$ kg/m³ contour in Fig. 8 is close to the critical density $\rho_{crit} \sim 375$ kg/m³ [71] and thus roughly visualizes the boundary between liquid metal and dense vapor. Low ρ in the crater results in a corresponding low σ, and hence the crater plays a similar role to the original pit, forcing **j** to divert around [as sketched in Fig. 8(c)] and amplify at the crater's equator. Consequently, just as **j** redistribution resulted in a region of enhanced j^2/σ encircling the pit [Fig. 3(f)], the same can be seen in the crater [blue dashed contour in Fig. 8(j)]. Enhanced j^2/σ at the edge of the crater/HS [Fig. 8(d)] will overheat higher-ρ metal there, causing it to explode, thus continuously widening and deepening the crater/HS. As a result, the corresponding visible emission pattern in Fig. 8(e) has broadened relative to its earlier-time counterpart in Fig. 7(c), a result which has been experimentally confirmed in Ref. [42].

Now consider the HS once they expand past the rod surface, so they are no longer surrounded by melted metal but rather low-ρ, low-σ vapor, as in Figs. 8(f)–8(h). With the exception of the higher-ρ, higher-σ metal protrusions, the HS (bounded by the magenta $T = 1.1 \times 10^4$ K contour with squares) represent local *peaks* in σ [Fig. 8(g)] relative to the surrounding vapor; the HS have expanded sufficiently that now the dependence of σ on T changes sign relative to the solid or liquid case (i.e., $d\sigma_{HS}/dT > 0$). Hence, in contrast to Fig. 8(c), where the HS represented minima in σ (relative to surrounding metal), forcing **j** to redistribute around, now the HS represent local peaks in σ. Consequently, the HS can satisfy the feedback loop required for the filament form of ETI (see Appendix A): $\delta T_{HS} > 0 \Rightarrow \delta\sigma_{HS} > 0 \Rightarrow \delta j_{HS} > 0 \Rightarrow \delta(j^2/\sigma)_{HS} > 0$ [Fig. 8(h)] $\Rightarrow dT_{HS} > 0$. Just as in striation formation, **j** redistribution plays a vital role in HS and filament formation, now *concentrating* in the HS and providing enhanced j^2/σ to compete with pdV cooling during plume expansion.

In a "conventional" thermal explosion, the HS expand axially and azimuthally as they travel radially outward. Simulations also exhibit this behavior once the HS travel far enough away from the rod, as sketched by the white velocity vectors **v** in Figs. 8(a) and 8(k). However, within the metal, the HS initially *focus* azimuthally, once again due to the shaped-charge effect. As seen in Fig. 8(i), the crater resulting from the HS explosion generates a region of lower ρ and p, resulting in an azimuthally focusing $-\nabla p$, just as in the case of the pit [Fig. 5(b)]. Hence, newly heated material around the periphery of the crater [i.e., within the blue dashed curve in Fig. 8(j)], born in the presence of this $-\nabla p$, initially focuses azimuthally while expanding axially as it explodes. Figure 8(k) plots v_θ (m/s) overlaid with **v** vectors; as seen in the circled regions, **v** initially focuses azimuthally before expanding. The azimuthally focusing component of **v** is modest ($v_\theta \sim v_r/10$) but is sufficient to introduce a flow asymmetry in the expanding HS—in Fig. 8(f), the white **v** vectors show $v_z > v_\theta$. This flow asymmetry allows the HS to grow faster axially than azimuthally, as observed in Fig. 9(c), where we follow the HS in Fig. 8(f) at $t = 115$ to 125 ns—the HS transition to the axially elongated filaments predicted by ETI.

Relative to melted metal, the low-ρ plume is not an attractive current path, due to its low σ as well as its geometry,
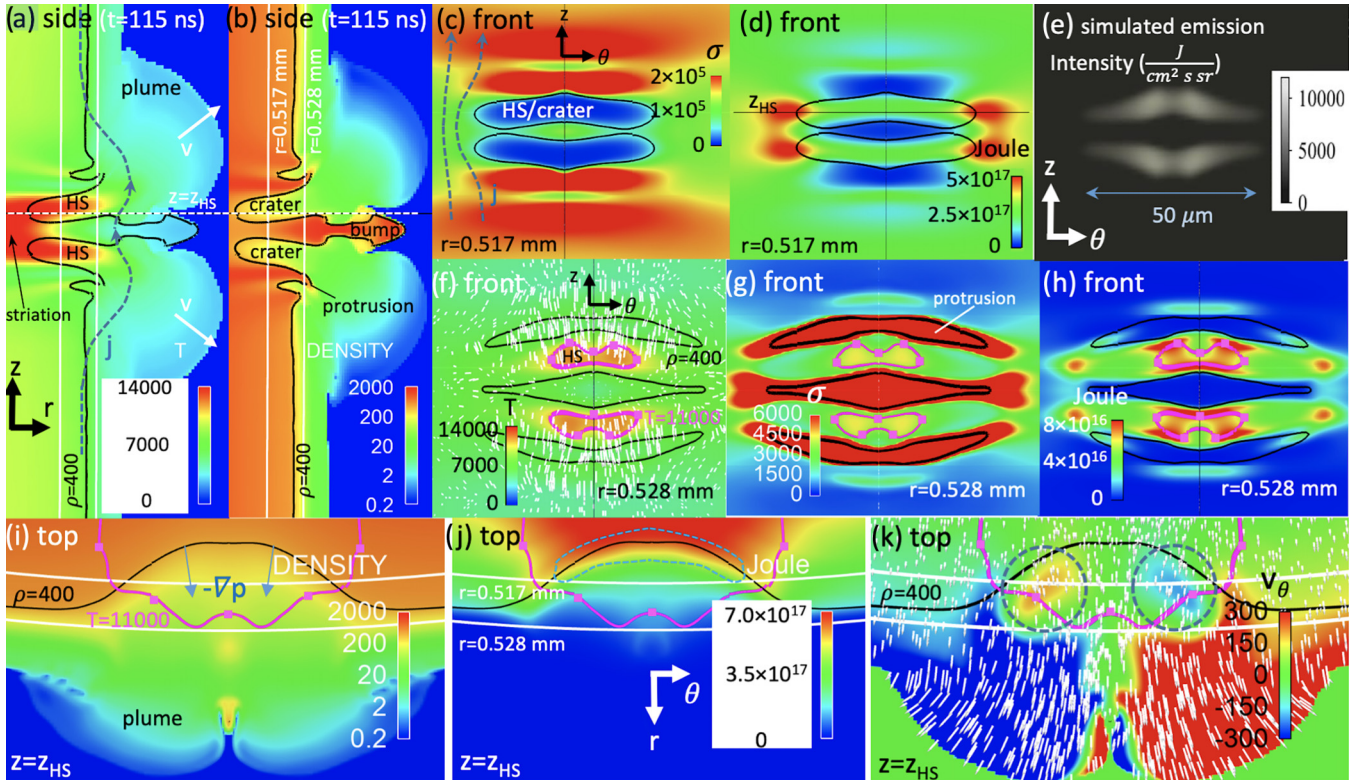
FIG. 8. [(a) and (b)] At $t = 115$ ns, the hot spots (HS) have exploded, resulting in expanding plumes as well as craters on the rod surface (visualized by the $\rho = 400$ kg/m^3 solid contour). White vertical lines show $r = 0.517$ and 0.528 mm. [(c) and (d)] Front views of HS/crater at $r = 0.517$ mm. (e) Simulated visible emission. [(f)–(h)] Front views at $r = 0.528$ mm show conditions for ETI filamentation in the HS, bounded by the $T = 1.1 \times 10^4$ K contour (with squares). In (f), the white velocity vectors illustrate flow asymmetry $v_z > v_\theta$, leading to filaments. The $z_{HS} = 100$ μm plane cuts through a hot spot and is shown in top view in (i)–(k). In (k), velocity vectors azimuthally focus in circled regions, due to the the shaped-charge effect. Units are T (K), ρ (kg/m^3), σ (1/Ωm), j^2/σ (W/m^3), and v_θ (m/s).

requiring **j** to bend radially outwards [see **j** streamline in Fig. 9(b)]. Just as in hydrodynamic flow over a bump (see Appendix B), **j** diminishes as it travels deeper into the plume. Hence, relatively little j flows in the HS as they expand outwards. Nevertheless, due to $d\sigma/dT > 0$, σ in the HS is enhanced relative to the surrounding liquid-vapor mixture. The resulting $\delta j_{HS} > 0$ [Fig. 9(d)] and $\delta(j^2/\sigma)_{HS} > 0$ allow the HS to maintain $T \sim$ const as they expand, despite pdV cooling. Hence, comparing Figs. 8(f) and 9(c), the liquid-vapor mixture (which does not experience enhanced j^2/σ) cools from $t = 115$ to 125 ns, while T_{HS} is approximately constant.

Enhanced j^2/σ in the HS allows the constituent fluid particles to develop into plasma significantly earlier than an equivalent 1D simulation (which models a perfectly smooth rod using the same radial resolution as 3D) by following a qualitatively different trajectory in the equation of state. To see this, Fig. 10(a) visualizes the equation of state in (p, ρ) space. The black lines, representing isotherms $T =$ const, become flat in the liquid-vapor biphase (i.e., coexistence) region, as is commonly described in textbooks (e.g., Refs. [78,79]). Consider the path $\mathcal{P}$ crossing the biphase region along an isotherm. At the rightmost (i.e., liquid) boundary of $\mathcal{P}$, we imagine a sealed container with a fixed mass of fluid. As we increase the container volume, the fluid separates into a boiling liquid-vapor mixture, so that the average density in the container decreases (corresponding to moving to the left

along $\mathcal{P}$). As we further increase the container volume, the vapor pressure remains constant since the extra volume is filled with additional vapor, which comes at the expense of the fluid mass. To remain on the isotherm $\mathcal{P}$ requires constant energy input, to counteract pdV cooling during expansion, as well as to vaporize liquid into vapor. Eventually, the container expands sufficiently to reach the left boundary of $\mathcal{P}$, where the fluid has converted completely into vapor. The total energy supplied to cross $\mathcal{P}$ from liquid to vapor is the latent heat of vaporization $\mathcal{L}_V$. Once this energy has been "paid," subsequent energy input can go towards increasing thermal energy (i.e., T) rather than towards phase transition.

Figure 10(a) visualizes the equivalent 1D simulation at three different times to illustrate the plasma formation process in the absence of 3D ETI, which has been studied in detail in previous works [80–82]. Each red cross represents (p, ρ) in a computational cell at $t = 115$ ns. As the liquid metal expands, the surface reaches lower ρ and also cools (thus crossing isotherms), signaling that pdV cooling exceeds Joule heating. At $t = 115$ ns the surface has cooled sufficiently that it has entered the biphase region. At $t = 125$ ns (green diamonds), outermost cells continue to cool and expand (lower ρ and T) but eventually carry sufficient j that Joule heating exceeds pdV cooling. However, as described earlier, the added energy goes primarily into $\mathcal{L}_V$ rather than increasing T; cells are "trapped" in the biphase region until the entirety of $\mathcal{L}_V$ has been supplied. By $t = 148$ ns (blue triangles), the outermost
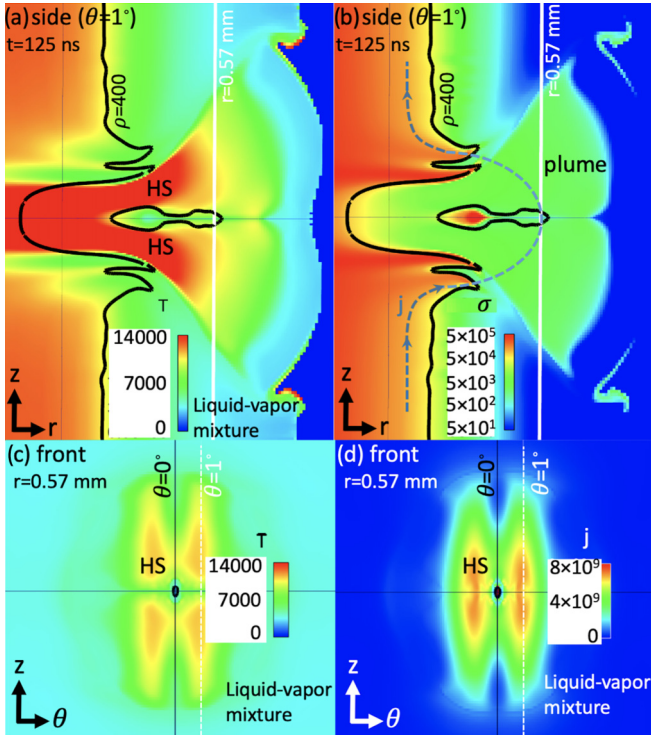
FIG. 9. As the HS explode, they grow preferentially in the axial (i.e., $\hat{z}$) direction, thus transitioning toward ETI filaments by $t = 125$ ns. Unlike the other side views in this paper, (a) and (b) do not visualize the center of the computational mesh (i.e., $\theta = 0°$), but rather $\theta = 1°$, to show the axial elongation of the HS. Units are T (K), σ (1/Ωm), and j (A/m^2).
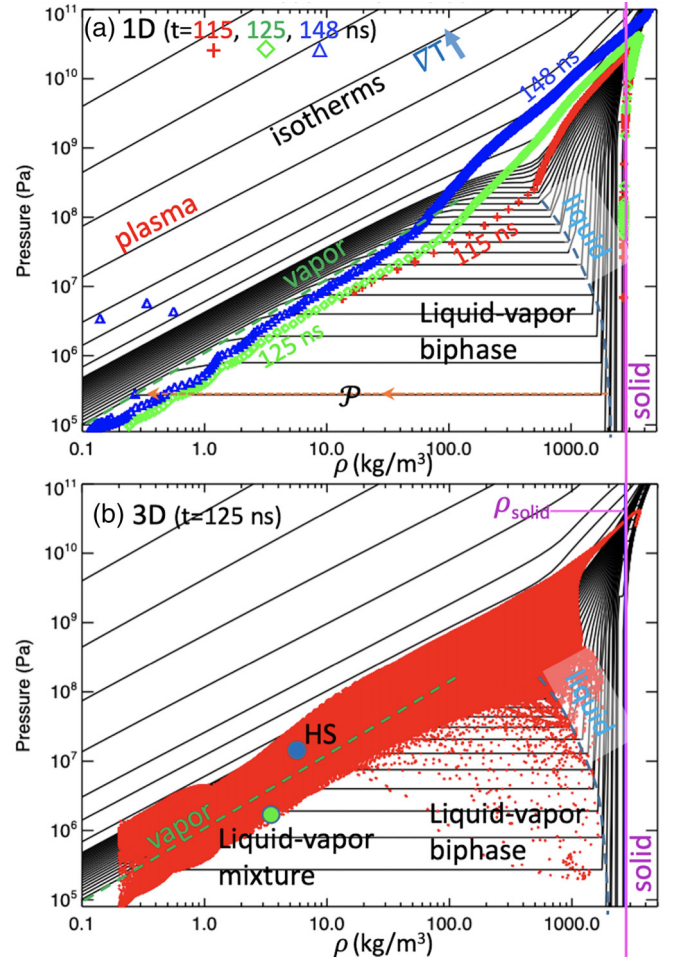

FIG. 10. (a) Phase plot for aluminum. Solid black lines are isotherms. Each symbol represents (p, ρ) in a computational cell in a 1D simulation, with red crosses, green diamonds, and blue triangles corresponding to $t = 115$, 125, and 148 ns, respectively. (b) (p, ρ) pairs from the 3D simulation at $t = 125$ ns. The upper blue circle shows the approximate location of HS cells in Fig. 9(c), while the lower green circle corresponds to surrounding liquid-vapor mixture. Due to ETI-enhanced j^2/σ, the HS avoid the biphase region, leading to earlier plasma formation than the 1D case.

cells have expanded and heated sufficiently that they have finally escaped the biphase region, reaching the vapor boundary [see green dashed line on left-hand side of Fig. 10(a)]. At this point, since the phase change from liquid to vapor is complete, additional heating goes toward raising T, allowing the outermost cells to heat rapidly to $T \sim 3 \times 10^4$ K.

Figure 10(b) overlays (p, ρ) pairs from the 3D simulation at $t = 125$ ns. The lower green circle roughly corresponds to cells constituting the liquid-vapor mixture surrounding the HS, shown in Fig. 9(c). Similarly to the 1D case at $t = 125$ ns, the liquid-vapor mixture cools as it expands, eventually falling into the biphase region. In contrast, the HS follow a qualitatively different trajectory in (p, ρ) space. Because of the azimuthally focused j and resulting ETI-enhanced j^2/σ (which cannot be modeled in 1D), as the HS expand, they are able to maintain $T\sim$const despite pdV cooling. As a result, the HS remain "above" the biphase region, so once $j^2/\sigma > pdV$, the HS can heat rapidly.

The significance of this observation is seen at $t = 135$ ns, when the expanding plume has spanned the axial extent of the computational domain [Fig. 11(a)]. Recalling from Fig. 2(b) that our computational scenario treats a single pit in a periodic array, **j** can flow through axially neighboring plumes without having to bend radially out of the rod [compare **j** streamline in Figs. 9(b) and 11(a)]. At this point, **j** carried in the plume increases sharply, and the resulting j^2/σ boosts the filaments to plasmalike temperatures [compare Fig. 11(d) and Fig. 9(c)],

which dominates self-emission in Fig. 11(h). Because Joule heating in the filament can go directly into increasing T rather than supplying $\mathcal{L}_V$, the filament achieves plasmalike temperatures $\sim$17 ns earlier than the equivalent 1D simulation shown in Fig. 10(a).

In Ref. [82], researchers simulated 1D plasma formation as applied to a similar experimental scenario, 1 MA electrical current applied to aluminum rods of various diameter. Using LMD conductivities similar to those used here, they found that 1D simulation forms plasma significantly later than experiment (e.g., $\sim$14 ns later for 1-mm-diameter rods). The 3D ETI-assisted Joule heating mechanism described here may help explain this discrepancy, since experimental self-emission shows plasma forming via 3D filaments [1,20,39,40,83], rather than in a 1D uniform sense.

Inside the metal, the striation has continued to overheat and widen [compare Figs. 11(e) and 7(d)] through the **j**
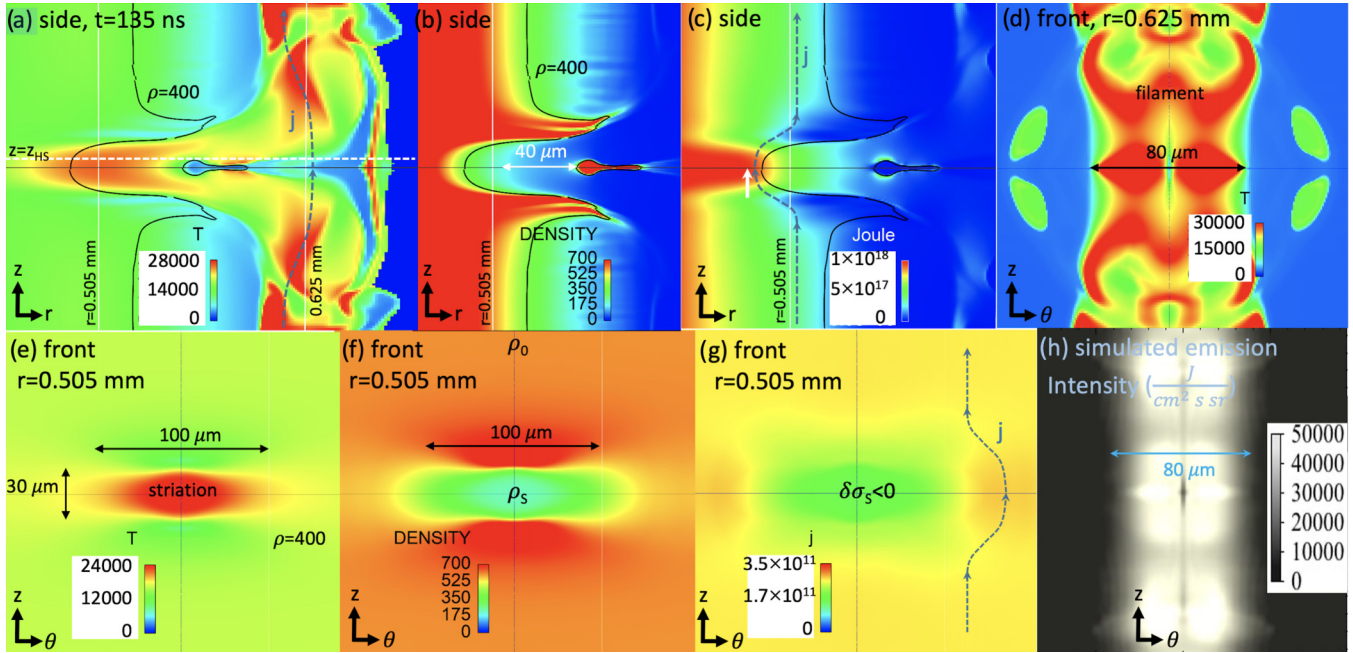
FIG. 11. At $t = 135$ ns, the plume spans the computational domain axially, increasing j carried in the filament and leading to rapid Joule heating. The filament, visualized in (a) and (d), dominates self-emission in (h). The striation, visualized in (e)–(g), coexists with the filament. Units are T (K), ρ (kg/m^3), j^2/σ (W/m^3), and j (A/m^2).

redistribution process described earlier. The striation and filament are spatially large enough that estimates of thermal conduction losses are again negligible relative to Joule heating, similarly to the case of early-time pit overheating illustrated in Figs. 4(a) and 4(b). Due to the expulsion of overheated material through the plumes, the striation also corresponds to a region of significantly lower ρ, as seen in Fig. 11(f). For instance, ρ at the center of the striation (identified by ρ_S) is 2.6× lower than the unperturbed value ρ_0. Hence, the pit has seeded a crater that is roughly 4× deeper [Fig. 11(b)] and 5× wider than the original pit size, providing a seed for the magneto-Rayleigh-Taylor instability, as demonstrated in Ref. [43]. The low-σ striation will continue to widen, due to **j** deflecting azimuthally [see Fig. 11(g)], causing a local enhancement in j and j^2/σ at the edge. The striation will also continue to deepen, due to **j** bending radially [see **j** streamline in Fig. 11(c)], resulting in enhanced j and j^2/σ behind the striation [see white arrow in Fig. 11(c)].

Finally, Fig. 12 shows top views of j and B, along with **B** streamlines. While the filament carries enhanced j relative to the surrounding liquid-vapor mixture, the fraction of total current carried by the filament $I_{fil}/I < 1\%$ is too small to noticeably perturb B in Fig. 12(b). In particular, **B** streamlines do not encircle the filament (which would be the case when I_{fil} is a significant fraction of total current I), thus precluding the possibility of filament self-pinching through the **j** × **B** force.

V. CONCLUSION

Three-dimensional MHD simulations illustrate how a hemispherical pit on a metal surface initiates a complex 3D feedback loop involving **j** and σ: Regions of enhanced j and Joule heating exhibit higher T and lower ρ (due to hydrodynamic expansion), altering the $\sigma(\rho, T)$ topography, which

causes **j** to redistribute. Consequently, **j** constantly shifts as it both reacts to and alters the ever-changing σ, transforming the pit into a bump, which then overheats to create exploding plumes and residual craters.

In solid or liquid metal, an overheated, expanded region $\mathcal{O}$ exhibits *negative* feedback: Higher T and lower ρ drive lower σ, which causes **j** (the source of overheating) to migrate out of $\mathcal{O}$ and amplify at the edges. The resulting enhanced Joule heating allows $\mathcal{O}$ to grow in a direction transverse to the axially flowing, unperturbed current by overheating surrounding material. Hence, negative feedback in solid or liquid metal encourages spatial growth through **j** redistribution. Despite reduced j in $\mathcal{O}$, enhanced Joule heating there is still
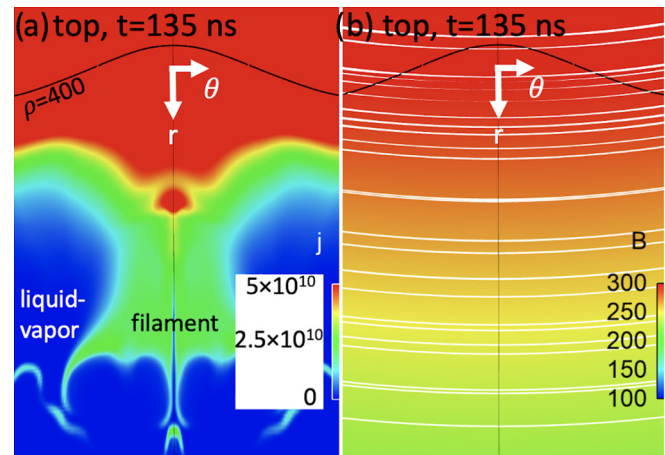

FIG. 12. Top views of j (A/m^2) and B (T), visualizing $z_{HS} = 100$ μm [see Fig. 11(a) for location]. Black lines represent $\rho = 400$ kg/m^3 and nearly horizontal white curves in (b) are magnetic streamlines.

possible if the enhancement due to reduced σ overcomes the reduction due to reduced j [as in Fig. 7(h)]. Through these processes, an initially localized resistive perturbation (the pit) seeds the development of a wide, hot strip (the ETI striation), which is an important seed for the magneto-Rayleigh-Taylor instability. Throughout the many flow patterns exhibited by **j** during this feedback-driven evolution, the analogy between **j** and hydrodynamic flow provides insight.

Once material expands into the vapor phase, as in the exploding plumes, $d\sigma/d\rho$ becomes negligible compared to $d\sigma/dT$ (see Fig. 1). Because $d\sigma/dT > 0$ in vapor, an over-heated region $\mathcal{O}$ will now experience *positive* feedback: Higher T generates higher σ, which in turn encourages higher j and increased Joule heating. Hence, now **j** tends to *focus* into $\mathcal{O}$, rather than divert around, so **j** redistribution no longer drives spatial growth transverse to unperturbed current flow. However, as seen in Sec. IV, the overheated HS still grow spatially, now through hydrodynamic expansion rather than **j** redistribution. Due to the shaped-charge effect, the HS grow preferentially in the axial direction, transforming them into the elongated plasma filaments predicted by ETI theory. While **j** redistribution does not directly determine HS spatial growth, it nevertheless plays an important role: Enhanced j and Joule heating in the HS (due to **j** redistribution) counteracts pdV cooling more effectively than in an equivalent 1D radially resolved simulation. Consequently, in 3D, HS fluid particles follow a different trajectory in (p, ρ) space, avoiding the liquid-vapor biphase region. As a result, for the scenario treated here, plasma forms $\sim$17 ns earlier in 3D compared to 1D, thus illustrating the important role of 3D **j** redistribution in plasma formation.

Simulations rely heavily on equation-of-state and electrical conductivity tables, as well as 3D hydrodynamics. Furthermore, most of the processes occur in the difficult-to-model warm dense matter regime (e.g., Refs. [84,85]), underscoring the need for experimental validation. While experiments involving current-driven metal rods indeed show a connection between initial surface features and later-time emission [1,40], testing the predictions presented here—namely detailed self-emission patterns driven by a single 3D pit—requires special effort. Naturally occurring defects in metals are μm scale, so the resulting emission is below the resolution limit of most cameras. Furthermore, because there are so many defects, with unknown distribution (surface characterization cannot discern buried defects), the resulting emission images are very complicated, making interpretation difficult. Efforts to carefully track individual inclusions from preshot characterization to self-emission showed no clear one-to-one correspondence [86].

Recent experiments strived to understand the emission from isolated 3D defects by enforcing as unambiguous an initial condition as possible [42]. Using 99.999% pure aluminum rods (effectively no native inclusions or voids) with ultrasmooth ($\sim$10 nm) surface finishes (to minimize emission from machining grooves), pits were machined on the surface to seed the feedback loop discussed in this paper. While the quasihemispherical pits (12- and 24-μm diameters) are larger than typical voids encountered naturally, they are large enough to experimentally resolve detailed emission features. Furthermore, if the similarity principle (mentioned in the Introduction) holds, then large pits serve as surrogates for smaller voids in the sense that the initial **j** redistribution driven by large and small pits is the same, up to a spatial scale size. However, this surrogacy may be broken by thermal conduction: As estimated in the Supplemental Material to Ref. [43], thermal conduction losses are expected to be negligible for a 10-μm-scale pit but significant for a 1-μm pit.

As mentioned previously, these experiments show promising agreement with the emission patterns predicted in Figs. 7(c), 8(e), and 11(h). Since these patterns reflect the shifting Joule heating peaks and associated hydrodynamics, the agreement gives us confidence in the basic adequacy of MHD modeling, albeit for a very specific case, 24-μm quasihemispherical pits on the surface of a 1-mm-diameter aluminum rod driven with $\sim$1 MA current. We have started testing the robustness of the results by simulating pits filled with dielectric (to mimic resistive inclusions), tilted ellipsoidal pits (to break the symmetry imposed by a hemisphere), higher $\frac{dI}{dt}$ current pulses, and MagLIF-like [22–27] liners driven by 20-MA current. While this is only a small subset of possible variations, all cases show qualitatively similar behavior, in particular developing the larger striation and filament structures. This result suggests that the physical processes described here—3D structure evolution driven by dynamic **j** and j^2/σ, coupled with hydrodynamics—have a universal character and constitute building blocks toward a 3D theory of defect evolution in current-driven metal.

Although we conclude our discussion here, many questions remain. For instance, given that metals commonly contain plentiful 3D defects (e.g., voids and inclusions), how do defects communicate through **j** redistribution to coalesce into larger structures? What is the effect of different materials? How do defect-driven ETI and the magneto-Rayleigh-Taylor instability interact in imploding systems? Are non-MHD effects important in the low-density plume? Regarding this final question, in the plasma filament the drift velocity $u_d \equiv v_e - v_i = -j/en_e$, measuring the difference between electron velocity v_e and ion velocity v_i, is indeed comparable to the fluid velocity v. This condition can signify the onset of Hall effects (e.g., see discussion in Ref. [44]) as well as anomalous resistivity (e.g., Ref. [87]), and indeed some experimental observations of filament evolution have so far defied explanation by MHD simulation. Finally, on higher current pulsed-power accelerators, we should consider the role of contaminant plasmas (generated in the magnetically insulated transmission lines) striking the metallic target, thus providing an additional seed for ETI [88,89]. In summary, the 3D evolution of current-driven metal is a largely unexplored, physically rich subject that invites further experimental, numerical, and theoretical investigation.

APPENDIX A: ETI SUMMARY

In this section, we review the fundamentals of the ETI, which is a heating instability that occurs whenever electrical conductivity σ depends on temperature T. For purposes of this discussion, it will be more convenient to work with the electrical resistivity $\eta \equiv 1/\sigma$. In the case of solid or liquid metals, where $d\eta/dT > 0$, the physical basis of the instability can be roughly described as follows: A hotter region will have higher η, leading to enhanced Joule heating ηj^2 (under certain conditions, to be clarified below), which drives the region even hotter. ETI can also occur when $d\eta/dT < 0$, as in the vapor or plasma phase: Hotter regions have lower η, but higher current j (from Ohm's law $j = E/\eta$), which can lead to enhanced Joule heating, driving higher T.

To quantify the above arguments, we briefly review the analysis of Ref. [15], which considers a planar shell with vertical current j_z, generating horizontal magnetic field B_y, as in Fig. 13(a). The shell thickness ΔR is assumed sufficiently thin that current is fully diffused. We assume small perturbations of the form $e^{\gamma t + ik_y y + ik_z z}$, where **k** is the wave vector forming an angle α with the magnetic field and γ is the ETI instability growth rate. Such a perturbation results in alternating hot and cold bands, as illustrated in Fig. 13(a). In the simplest case where we ignore thermal conduction and hydrodynamic expansion, we can estimate a typical value of the ETI timescale $\gamma^{-1} \sim \rho c_V /(\frac{d\eta}{dT} j^2)$ in aluminum prior to melt. Approximating $\frac{d\eta}{dT} \sim 1.2 \times 10^{-10}$ Ωm/K, $j \sim 1 \times 10^{12}$ A/m^2, $\rho \sim 2700$ kg/m^3, $c_V \sim 920$ J/kgK, we find $1/\gamma \sim 21$ ns.

Even in this 2D geometry, current redistribution $\delta\mathbf{j}$ plays an important role. Taking the z component of the perturbed Ohm's law, we find

$$\delta j_z = -\frac{\delta\eta}{\eta} j_z + \frac{1}{\eta}\delta E_z, \tag{A1}$$

where the first term represents how δj_z responds to $\delta\eta$ (i.e., region of enhanced resistivity $\delta\eta > 0$ results in reduced j_z), whereas the second term is the contribution to δj_z from the
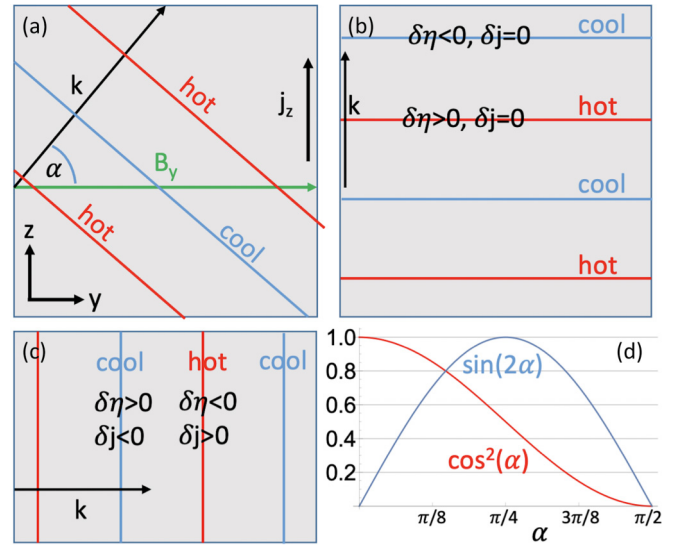

FIG. 13. (a) ETI planar analysis. The y coordinate corresponds to azimuthal coordinate θ in cylindrical geometry. (b) Striation form of ETI in metal ($d\eta/dT > 0$). (c) Filament form of ETI in vapor ($d\eta/dT < 0$). (d) Dependence of δj_y (blue) and δj_z (red) on angle α.

induced electric field, satisfying Faraday's law,

$$\nabla \times \delta\mathbf{E} = -\frac{\partial\delta\mathbf{B}}{\partial t}. \tag{A2}$$

As shown in Ref. [15], combining Ampère's law with Eq. (A2) allows us to express δj_z in terms of $\delta\eta$:

$$\delta j_z = -\frac{j_z \cos^2\alpha}{1 + \gamma\tau_R}\frac{\delta\eta}{\eta}, \tag{A3}$$

where $\tau_R \equiv \frac{\mu_0\Delta R}{2k\eta}$ is a resistive diffusion timescale for perturbations of wavelength $\lambda = 2\pi/k$ and radial extent ΔR. Also, charge conservation $\nabla \cdot \delta\mathbf{j} = 0$ requires

$$\delta j_y = -\frac{k_z}{k_y}\delta j_z. \tag{A4}$$

Combining Eqs. (A3) and (A4), noting $\cos\alpha = k_y/k$ and $\sin\alpha = k_z/k$, we can rewrite

$$\delta j_y = \frac{j_z}{2}\frac{\sin 2\alpha}{1 + \gamma\tau_R}\frac{\delta\eta}{\eta}. \tag{A5}$$

Note that if $\alpha = \pi/2$, corresponding to the striation form of ETI [see Fig. 13(b)], $\delta j_y = \delta j_z = 0$; there is no current redistribution because **j** cannot flow "around" the $\delta\eta > 0$ regions, which span the plane. Conversely, if $\alpha = 0$, corresponding to the filament form of ETI [as in Fig. 13(c)], then $\delta j_y = 0$ and

$$\delta j_z = -\frac{j_z}{1 + \gamma\tau_R}\frac{\delta\eta}{\eta}, \tag{A6}$$

i.e., now current redistribution is nonzero, with **j** preferentially flowing in the lower resistivity $\delta\eta < 0$ filaments.

The $\alpha = 0$ case provides a simple illustration of the importance of the induced electric field δE_z in determining **j** redistribution. If we simply ignored δE_z, then Eq. (A1) yields $\delta j_z = -\frac{\delta\eta}{\eta} j_z$. Comparing to Eq. (A6), which *does* account for δE_z, we see that the effect of δE_z is to reduce δj_z by the

factor $(1 + \gamma \tau_R)^{-1}$. Recall δE_z captures the Faraday effect, so **j** responds to changes in $\delta \eta$ not instantaneously but rather on the resistive diffusion timescale τ_R. Hence, if $\gamma \tau_R \gg 1$, then $\delta j_z \to 0$, i.e., **j** is frozen, because the timescale τ_R for **j** redistribution is long relative to the instability timescale γ^{-1}. Conversely, if $\gamma \tau_R \ll 1$, then the effect of δE_z is negligible: γ^{-1} is so long compared to τ_R that δj_z effectively redistributes instantaneously to the value $\delta j_z = -\frac{\delta \eta}{\eta} j_z$.

Let us now seek a simple physical explanation for why horizontal striations naturally occur in solid or liquid metals, while vertical filaments appear in the vapor or plasma phase. The perturbed Ohmic heating yields

$$\delta(\eta j^2) = \delta \eta j^2 + 2\eta j \delta j, \tag{A7}$$

where

$$j = \sqrt{(j_z + \delta j_z)^2 + \delta j_y^2} \simeq j_z + \delta j_z \tag{A8}$$

and

$$\delta j \simeq \delta j_z, \tag{A9}$$

with Eq. (A9) and the final equality in Eq. (A8) being valid to first order. Equations (A3), (A7), (A8), and (A9) can be combined to yield

$$\delta(\eta j^2) = \delta \eta j^2 + 2\eta j \delta j \simeq \delta \eta j^2 \left(1 - \frac{2\cos^2 \alpha}{1 + \gamma \tau_R} \right). \tag{A10}$$

In the limit $\gamma \tau_R \ll 1$,

$$\delta(\eta j^2) = \delta \eta j^2 + 2\eta j \delta j \simeq \delta \eta j^2 (1 - 2\cos^2 \alpha). \tag{A11}$$

Consider the condition for instability as applied to Eq. (A11). In order for instability to grow, a region of enhanced temperature $\delta T > 0$ must have enhanced Joule heating $\delta(\eta j^2) > 0$ so that δT can be driven even higher. Let us first consider a metal so that $\delta \eta > 0$ in the hot spot. Then the first term $\delta \eta j^2$ in Eq. (A11) is positive, and hence drives instability, but must compete with the stabilizing second term $2\eta j \delta j$, which is negative owing to $\delta j < 0$ in the region $\delta \eta > 0$. Therefore, maximum growth rate is achieved by minimizing the stabilizing term proportional to δj, which from Eq. (A11) occurs for $\alpha = \pi/2$. Physically, this scenario corresponds to the horizontal hot and cold bands illustrated in Fig. 13(b).

Having explained why striations are the most virulent instability in the solid or liquid phase, we now consider the vapor or plasma phase, where $d\eta/dT < 0$ and the filament form of ETI dominates. Now a hotter region has lower η, and for ETI to grow, this region must have $\delta(\eta j^2) > 0$. Looking at Eq. (A11), the role of the terms is reversed from the previous discussion: Since $\delta \eta < 0$ in the hot region, the first term is negative and stabilizing, whereas the second term is positive and destabilizing. Physically, reduced η in the hot region will reduce Joule heating but also amplify j, enhancing Joule heating. The maximum instability occurs when δj is maximized, which from Eq. (A11) occurs for $\alpha = 0$, thus resulting in the filaments of Fig. 13(c).

To complete our picture of current redistribution in the 2D system, we consider the general case $0 < \alpha < \pi/2$. Consider the metal phase where $d\eta/dT > 0$ and "striation-like" structures with $\pi/4 < \alpha < \pi/2$. In this case, Eqs. (A3) and (A5)
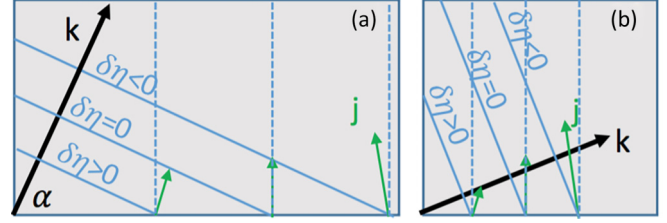

FIG. 14. Current redistribution in ETI planar analysis in (a) $\alpha > \pi/4$ and (b) $\alpha < \pi/4$, showing **j** in bands of varying resistivity. In regions of reduced resistivity $\delta \eta < 0$, j is amplified, and $\delta j_y < 0$, consistent with our intuition that **j** tries to flow *along* the band $\delta \eta < 0$. Conversely, when $\delta \eta > 0$, we see $\delta j_y > 0$: **j** tries to cross the region "quickly" by flowing nearly perpendicular.

show that δ**j** is nonzero. As illustrated in Fig. 14(a), regions of enhanced η have reduced δj_z and δj, but Eq. (A11) and Fig. 13(d) show that hot bands of $\delta \eta > 0$ still have $\delta \eta j^2 > 0$, i.e., current redistribution is not sufficient to stabilize the $\delta \eta > 0$ bands. Once $\alpha = \pi/4$, from Eq. (A5) the transverse current δj_y reaches a maximum ($|\delta j_y| = |\delta j_z|$) and current redistribution out of the $\delta \eta > 0$ region is sufficient to reach marginal stability in Eq. (A11), $\delta(\eta j^2) = 0$. Decreasing α still further to $\alpha < \pi/4$, as in Fig. 14(b), $|\delta j_z|$ increases to the point where now in the hotter $\delta \eta > 0$ regions, current redistribution is sufficient to drive $\delta(\eta j^2) < 0$ there, as seen in Eq. (A11). Hence, the instability is quenched: Hotter regions of $\delta \eta > 0$ have reduced Joule heating, thus breaking the positive feedback loop.

APPENDIX B: FLOW OVER BUMP OR DIVOT

In this section we review 2D current flow over a bump or divot, using the analogous hydrodynamic solution presented in the monograph by Milne-Thomson [41]. For the benefit of readers interested in studying Ref. [41] further, we maintain his notation. The solution is expressed in coaxal coordinates (η, ξ), related to Cartesian coordinates (x, y) through

$$\frac{x}{c} = \frac{\sinh \eta}{\cosh \eta - \cos \xi}, \tag{B1}$$

$$\frac{y}{c} = \frac{\sin \xi}{\cosh \eta - \cos \xi}, \tag{B2}$$

where c is an arbitrary constant that will parametrize the half-width of the bump or divot. Figure 15 plots contours of constant ξ (dashed lines), representing circles centered at $x = 0$, $y = c \cot \xi$ with radius $c|\csc \xi|$, which always intersect the x axis at $x = \pm c$. Consider a specific value of $\xi = \xi_0$ satisfying $0 < \xi_0 < \pi$. As seen in Fig. 15, this describes the portion of a circle lying above the x axis; to access the bottom portion of the circle at $y < 0$, we consider $\xi = \xi_0 + \pi$. Also, as $\xi \to 0$, the circle becomes so large and is centered so far above the x axis that it approximates the x axis (for $|x| > c$, as seen by the $\xi = \pi/100$ contour); points on the x axis satisfying $|x| < c$ are described by $\xi = \pi$. Curves of constant ξ provide a natural description of divots and bumps.

Contours of constant η represent circles centered at $x = c \coth \eta$, $y = 0$ with radius $c|\csch \eta|$. As $\eta \to 0$, the circle is
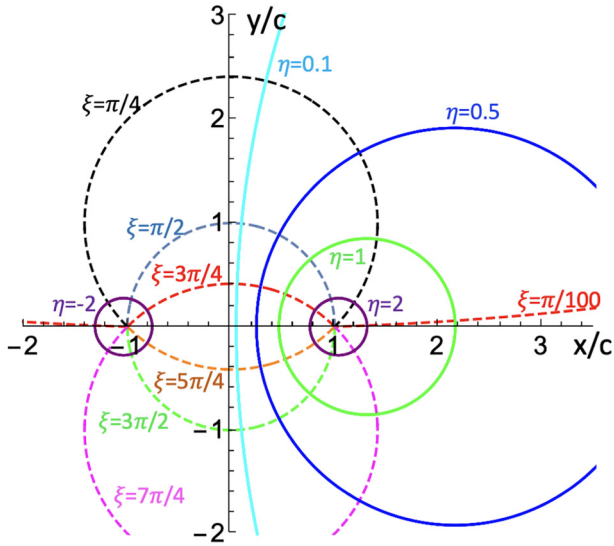
FIG. 15. Coaxal coordinates (ξ, η) used to study flow over a divot or bump. Dashed lines represent curves of constant ξ, while solid lines represent constant η. Each point in the (x, y) plane is associated with a unique (ξ, η) pair.

so large and centered so far from the origin that it approximates the y axis (see $\eta = 0.1$ curve in Fig. 15), whereas as $\eta \to \infty$, the circle shrinks to a point centered at $x = c$. Note that $\eta = \eta_0 > 0$ traces out a circle centered at $x_0 > 0$, whereas $\eta = -\eta_0$ traces out the mirror image of the circle, centered at $x = -x_0$ (compare $\eta = \pm 2$ in Fig. 15). Hence, we can associate any point in the (x, y) plane with a unique coaxal coordinate pair (η, ξ).

To connect to the problem of interest in this paper—axial current flow $\mathbf{j}_0$ flowing over a radially extended bump or divot—we associate x in Fig. 15 with the axial coordinate z and y with the radial coordinate $-r$. Hence, in the case of a perfectly smooth rod, the metal occupies $y > 0$, with vacuum in $y < 0$. To introduce a divot, we consider $\xi = \xi_0$ with $0 < \xi_0 < \pi$ describing a divot of varying radial depth and fixed axial half-width c. Conversely, $\pi < \xi_0 < 2\pi$ represents a bump.

For current flow $\mathbf{j}$ flowing over either a divot or bump, the solution is

$$\frac{j}{j_0} = \frac{4}{n^2} \left(\frac{\cosh \eta - \cos \xi}{\cosh \frac{2\eta}{n} - \cos \frac{2\xi}{n}} \right), \tag{B3}$$

where j_0 is the value of j infinitely far from the divot or bump (flowing in the $\hat{x}$ direction) and n characterizes the shape and depth of the divot or bump through $\xi_0 = n\pi/2$. Hence, $0 < n < 2$ (i.e., $0 < \xi_0 < \pi$) describes a divot while $2 < n < 4$ (i.e., $\pi < \xi_0 < 2\pi$) describes a bump.

Figure 16 illustrates the solution for $\xi_0 = 3\pi/2$, corresponding to a semicircular bump with depth δy equal to half-width c. The unperturbed metal occupies $y > 0$; we only plot j in the bump. At the base of the bump ($x = \pm c, y = 0$), the metal surface makes an abrupt $90°$ turn, causing $\mathbf{j}$ streamlines to bunch up as $\mathbf{j}$ is pulled into the bump. Consequently, j achieves its maximum value, in fact approaching ∞. This unphysical singularity is well known in the theory of plane
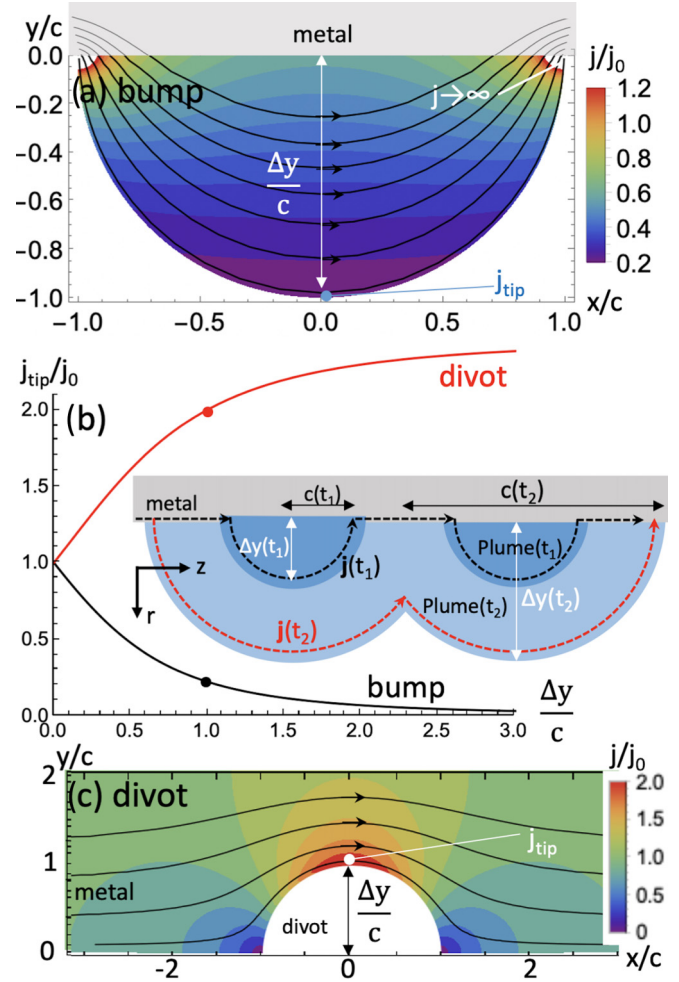

FIG. 16. (a) Flow of $\mathbf{j}$ over bump, described by $\xi_0 = 3\pi/2$. Coloring represents j/j_0, where j_0 is the value of j infinitely far from the bump, and black lines are $\mathbf{j}$ streamlines. At the corners $(x/c = \pm 1, y = 0)$, $j \to \infty$. (b) Solution for j_{tip}/j_0 as a function of aspect ratio $\Delta y/c$ for both bump and divot. The black and red dots correspond to the solution for the bump shown in (a), and the divot in (c), respectively. The inset illustrates a plume connection scenario, leading to enhanced j carried in the plume, as described in the text. (c) Flow of uniform stream over divot, described by $\xi_0 = \pi/2$.

ideal (i.e., zero viscosity) hydrodynamic flow around a convex corner (e.g., see Sec. 18.2 in Ref. [90]). Here the singularity vanishes when additional viscous physics is added, effectively smoothing the corner.

In a conducting metal, as suggested in Ref. [10], in reality the corner will be rounded rather than perfectly sharp, thus resolving the singularity. Even in the idealized case of a sharp corner, the singularity in j will rapidly resolve itself by heating the corner, with the corresponding drop in σ effectively smoothing the corner. Finally, the solution in Fig. 16(a) assumes that the bump (at $y < 0$) and overlying metal (at $y > 0$) have the same electrical conductivity σ. However, in both cases in this paper in which the bump solution is applicable— when the pit converts to a bump (Fig. 6) and when hot spots explode to form plumes (Fig. 8)—the protrusion has lower σ than the rod, which will further prevent the singularity in j. However, the bump solution still provides important physical

insight: Figures 6(b) and 6(e) clearly show localized peaks in j at the predicted locations.

One measure of j in the bump is its minimum value at the tip, j_{tip} [see Fig. 16(a)]. Figure 16(b) plots j_{tip}/j_0 as a function of the aspect ratio $\Delta y/c$, where Δy is the bump depth and c is the half-width. As the bump deepens and $\Delta y/c$ increases, j_{tip} decreases, since it is "harder" for j to reach the tip. This dependence on $\Delta y/c$ provides a geometrical means for a current-carrying plasma plume [e.g., see Fig. 8(a)] to increase j when it merges with another plume. As illustrated in the inset of Fig. 16(b), bumps corresponding to exploding plasma or vapor plumes from two axially separated pits are initially separated at time t_1. Current follows the streamline $\mathbf{j}(t_1)$, with each plume pulling $\mathbf{j}$ outward, as determined by $\frac{\Delta y}{c}(t_1)$. As the plumes expand radially and axially, they eventually merge at time t_2. The resulting smaller $\frac{\Delta y}{c}(t_2)$ makes the merged plume a more accessible current path, increasing j_{tip} as well as j throughout the plume. This process is demonstrated numerically and supported experimentally in Ref. [42].

Last, Fig. 16(c) illustrates the solution for uniform current $\mathbf{j}_0$ flowing over a divot, described by the coaxal coordinate $\xi_0 = \frac{n\pi}{2} \to \pi/2$ [hence $n = 1$ in Eq. (B3)]. Unlike the bump, j is finite over the entire domain, reaching a maximum at the tip of the divot. For this particular value of ξ_0, describing a semicircular divot, the solution is identical to hydrodynamic flow over a circular cylinder, reaching $j_{tip}/j_0 = 2$. More generally, current amplification depends on the ratio of depth to width $\Delta y/c$, with j_{tip}/j_0 initially increasing linearly with $\Delta y/c$:

$$\frac{j_{tip}}{j_0} \simeq 1 + \frac{4}{\pi}\frac{\Delta y}{c}, \quad \frac{\Delta y}{c} < \frac{1}{2}, \tag{B4}$$

as seen in Fig. 16(b). At larger $\Delta y/c$, the divot takes on a bulbous shape (see for instance $\xi = \pi/4$ in Fig. 15), and j_{tip}/j_0 increases more slowly. As described in the main text, j amplification at the tip of the divot results in enhanced Joule heating there, providing a means for craters in exploding metals to continuously deepen.

[1] T. J. Awe, E. P. Yu, K. C. Yates, W. G. Yelton, B. S. Bauer, T. M. Hutchinson, S. Fuelling, and B. B. McKenzie, IEEE Trans. Plasma Sci. **45**, 584 (2017).

[2] S. Kuyucak and R. I. L. Guthrie, Can. Metall. Quart. **28**, 41 (1989).

[3] T. Sakurai, Y. Kohmura, A. Takeuchi, Y. Suzuki, S. Goto, and T. Ishikawa, AIP Conf. Proc. **879**, 1380 (2007).

[4] H. Lamb, *Hydrodynamics*, 6th ed. (Dover, New York, 1932).

[5] E. P. Yu, T. J. Awe, K. R. Cochrane, K. C. Yates, T. M. Hutchinson, K. J. Peterson, and B. S. Bauer, Phys. Plasmas, **27**, 052703 (2020).

[6] L. D. Landau and E. M. Lifshitz, *Fluid Mechanics, 2nd edition* (Butterworth-Heinemann, Oxford, 1987).

[7] M. P. Desjarlais, J. D. Kress, and L. A. Collins, Phys. Rev. E **66**, 025401(R) (2002).

[8] H. Knoepfel, *Pulsed High Magnetic Fields* (North-Holland, Amsterdam, 1970).

[9] S. M. Ponomarev, USSR Comput. Maths. Math. Phys. **28**, 177 (1988).

[10] G. A. Shneerson, M. I. Dolotenko, and S. I. Krivosheev, *Strong and Superstrong Pulsed Magnetic Fields Generation* (de Gruyter, Berlin, 2014), p. 22.

[11] O. Schnitzer, Phys. Plasmas **21**, 082306 (2014).

[12] V. I. Oreshkin and S. A. Chaikovsky, Phys. Plasmas **19**, 022706 (2012).

[13] S. A. Chaikovsky, V. I. Oreshkin, I. M. Datsko, N. A. Labetskaya, D. V. Rybka, and N. A. Ratakhin, Phys. Plasmas **22**, 112704 (2015).

[14] M. G. Haines, J. Plasma Phys. **12**, 1 (1974).

[15] D. D. Ryutov, M. S. Derzon, and M. K. Matzen, Rev. Mod. Phys. **72**, 167 (2000).

[16] V. I. Oreshkin, Phys. Plasmas **15**, 092103 (2008).

[17] K. J. Peterson, D. B. Sinars, E. P. Yu, M. C. Herrmann, M. E. Cuneo, S. A. Slutz, I. C. Smith, B. W. Atherton, M. D. Knudson, and C. Nakhleh, Phys. Plasmas **19**, 092701 (2012).

[18] J. D. Pecover and J. P. Chittenden, Phys. Plasmas **22**, 102701 (2015).

[19] T. M. Hutchinson, T. J. Awe, B. S. Bauer, K. C. Yates, E. P. Yu, W. G. Yelton, and S. Fuelling, Phys. Rev. E **97**, 053208 (2018).

[20] A. M. Steiner, P. C. Campbell, D. A. Yager-Elorriaga, N. M. Jordan, R. D. McBride, Y. Y. Lau, and R. M. Gilgenbach, IEEE Trans. Plasma Sci. **46**, 3753 (2018).

[21] V. I. Oreshkin, R. B. Baksht, E. V. Oreshkin, A. G. Rousskikh, and A. S. Zhigalin, Plasma Phys. Control. Fusion **62**, 035016 (2020).

[22] S. A. Slutz, M. C. Herrmann, R. A. Vesey, A. B. Sefkow, D. B. Sinars, D. C. Rovang, K. J. Peterson, and M. E. Cuneo, Phys. Plasmas **17**, 056303 (2010).

[23] M. R. Gomez, S. A. Slutz, A. B. Sefkow, D. B. Sinars, K. D. Hahn, S. B. Hansen, E. C. Harding, P. F. Knapp, P. F. Schmit, C. A. Jennings *et al.*, Phys. Rev. Lett. **113**, 155003 (2014).

[24] M. E. Cuneo *et al.*, IEEE Trans. Plasma Sci. **40**, 3222 (2012).

[25] M. R. Gomez, S. A. Slutz, C. A. Jennings, D. J. Ampleford, M. R. Weis, C. E. Myers, D. A. Yager-Elorriaga, K. D. Hahn, S. B. Hansen, E. C. Harding *et al.*, Phys. Rev. Lett. **125**, 155002 (2020).

[26] D. A. Yager-Elorriaga *et al.*, Nucl. Fusion **62**, 042015 (2022).

[27] A. B. Sefkow, S. A. Slutz, J. M. Koning, M. M. Marinak, K. J. Peterson, D. B. Sinars, and R. A. Vesey, Phys. Plasmas **21**, 072711 (2014).

[28] M. M. Basko, A. J. Kemp, and J. Meyer-ter-Vehn, Nucl. Fusion **40**, 59 (2000).

[29] I. R. Lindemuth, Phys. Plasmas **22**, 122712 (2015).

[30] V. Mokhov, O. Burenkov, A. Buyko, S. Garanin, S. Kuznetsov, V. Mamyshev, A. Startsev, and V. Yakubov, Fusion Eng. Des. **70**, 35 (2004).

[31] P. F. Schmit and D. E. Ruiz, Phys. Plasmas **27**, 062707 (2020).

[32] E. G. Harris, Phys. Fluids **5**, 1057 (1962).

[33] Y. Zhou, Phys. Rep. **723-725**, 1 (2017).

[34] Y. Zhou, R. J. R. Williams, P. Ramaprabhu, M. Groom, B. Thornber, A. Hillier, W. Mostert, B. Rollin, S. Balachandar, P. D. Powell, A. Mahalov, and N. Attal, Physica D **423**, 132838 (2021).

[35] D. E. Ruiz, D. A. Yager-Elorriaga, K. J. Peterson, D. B. Sinars, M. R. Weis, D. G. Schroen, K. Tomlinson, J. R. Fein, and K. Beckwith, Phys. Rev. Lett. **128**, 255001 (2022).

[36] R. D. McBride, S. A. Slutz, C. A. Jennings, D. B. Sinars, M. E. Cuneo, M. C. Herrmann, R. W. Lemke, M. R. Martin, R. A. Vesey, K. J. Peterson *et al.*, Phys. Rev. Lett. **109**, 135004 (2012).

[37] P. A. Gourdain, M. B. Adams, M. Evans, H. R. Hasson, R. V. Shapovalov, J. R. Young, and I. West-Abdallah, Phys. Plasmas **26**, 042706 (2019).

[38] D. Zhang, J. Wu, Z. Chen, Y. Lu, H. Shi, G. Wang, D. Xiao, N. Ding, X. Li, S. Jia, and A. Qiu, Phys. Plasmas **27**, 062709 (2020).

[39] K. C. Yates, B. S. Bauer, S. Fuelling, T. J. Awe, T. M. Hutchinson, V. V. Ivanov, J. Mei, and R. S. Bauer, Phys. Plasmas **26**, 042708 (2019).

[40] K. C. Yates, T. J. Awe, B. S. Bauer, T. M. Hutchinson, E. P. Yu, S. Fuelling, D. C. Lamppa, and M. R. Weis, Phys. Plasmas **27**, 082707 (2020).

[41] L. M. Milne-Thomson, *Theoretical Hydrodynamics* (Dover, New York, 1968).

[42] T. J. Awe, E. P. Yu, M. W. Hatch, T. M. Hutchinson, K. Tomlinson, W. D. Tatum, K. C Yates, B. T. Hutsel, and B. S. Bauer, Phys. Plasmas **28**, 072104 (2021).

[43] E. P. Yu, T. J. Awe, K. R. Cochrane, K. J. Peterson, K. C. Yates, T. M. Hutchinson, M. W. Hatch, B. S. Bauer, K. Tomlinson, and D. B. Sinars, Phys. Rev. Lett. **130**, 255101 (2023).

[44] S. V. Lebedev, A. Frank, and D. D. Ryutov, Rev. Mod. Phys. **91**, 025002 (2019).

[45] J. E. Bailey, T. Nagayama, G. P. Loisel, G. A. Rochau, C. Blancard, J. Colgan, Ph. Cosse, G. Faussurier, C. J. Fontes, F. Gilleron *et al.*, Nature (Lond.) **517**, 56 (2015).

[46] R. W. Lemke, M. D. Knudson, D. E. Bliss, K. R. Cochrane, J.-P. Davis, A. A. Giunta, H. C. Harjes, and S. A. Slutz, J. Appl. Phys. **98**, 073530 (2005).

[47] S. N. Bland, Ya. E. Krasik, D. Yanuka, R. Gardner, J. MacDonald, A. Virozub, S. Efimov, S. Gleizer, and N. Chaturvedi, Phys. Plasmas **24**, 082702 (2017).

[48] M. D. Knudson, M. P. Desjarlais, A. Becker, R. W. Lemke, K. R. Cochrane, M. E. Savage, D. E. Bliss, T. R. Mattsson, and R. Redmer, Science **348**, 1455 (2015).

[49] K. J. Chung, K. Lee, Y. S. Hwang, and D. K. Kim, J. Appl. Phys. **120**, 203301 (2016).

[50] C. M. Fowler, Science **180**, 261 (1973).

[51] D. B. Sinars *et al.*, Phys. Plasmas **27**, 070501 (2020).

[52] Y. Maron, Phys. Plasmas **27**, 060901 (2020).

[53] A. Hubbard, C. P. McNally, and M. M. Low, Astrophys. J. **761**, 58 (2012).

[54] C. P. McNally, A. Hubbard, M. M. Low, D. S. Ebel, and P. D'Alessio, Astrophys. J. Lett. **767**, L2 (2013).

[55] R. A. Kerr, Science **341**, 126 (2013).

[56] S. W. Van Sciver, and K. R. Marken, Phys. Today **55**(8), 37 (2002).

[57] H. Padamsee, Supercond. Sci. Technol. **30**, 053003 (2017).

[58] S. Bao and W. Guo, Phys. Rev. Appl. **11**, 044003 (2019).

[59] P. Zhang, Y. Y. Lau, and R. M. Gilgenbach, J. Appl. Phys. **105**, 114908 (2009).

[60] A. VI. Gurevich and R. G. Mints, Rev. Mod. Phys. **59**, 941 (1987).

[61] A. L. Velikovich, A. J. Schmitt, C. Zulick, Y. Aglitskiy, M. Karasik, S. P. Obenschain, J. G Wouchuk, and F. Cobos Campos, Phys. Plasmas **27**, 102706 (2020).

[62] C. Zulick, Y. Aglitskiy, M. Karasik, A. J. Schmitt, A. L. Velikovich, and S. P. Obenschain, Phys. Rev. Lett. **125**, 055001 (2020).

[63] E. N. Loomis, D. Braun, S. H. Batha, C. Sorce, and O. L. Landen, Phys. Plasmas **18**, 092702 (2011).

[64] I. V. Igumenshchev, V. N. Goncharov, W. T. Shmayda, D. R. Harding, T. C. Sangster, and D. D. Meyerhofer, Phys. Plasmas **20**, 082703 (2013).

[65] A. B. Zylstra, D. T. Casey, A. Kritcher, L. Pickworth, B. Bachmann, K. Baker, J. Biener, T. Braun, D. Clark, V. Geppert-Kleinrath *et al.*, Phys. Plasmas **27**, 092709 (2020).

[66] B. M. Haines, J. P. Sauppe, B. J. Albright, W. S. Daughton, S. M. Finnegan, J. L. Kline, and J. M. Smidt, Phys. Plasmas **29**, 042704 (2022).

[67] G. Yagawa, S. Yoshimura, and Y. Akahoshi, Fusion Eng. Des. **7**, 269 (1989).

[68] E. Gallo, S. Satapathy, and K. Ravi-Chandar, Int. J. Fract. **167**, 183 (2011).

[69] D. Sharma, B. Subba Reddy, and P. Kumar, Int. J. Fract. **212**, 183 (2018).

[70] A. C. Robinson and C. J. Garasi, Comput. Phys. Commun. **164**, 408 (2004).

[71] T. Sjostrom, S. Crockett, and S. Rudin, Phys. Rev. B **94**, 144101 (2016).

[72] E. Kaselouris, V. Dimitriou, I. Fitilis, A. Skoulakis, G. Koundourakis, E. L. Clark, M. Bakarezos, I. K. Nikolos, N. A. Pagadogiannis, and M. Tatarakis, Nat. Commun. **8**, 1713 (2017).

[73] W. Neal, N. Sanchez, B. Jensen, J. Gibson, J. Romero, M. Martinez, C. Owens, D. Jaramillo, A. Iverson, C. Carlson, M. Teel, A. Derry, and P. Rigg, AIP Conf. Proc. **1979**, 180007 (2018).

[74] T. M. Hutchinson, T. J. Awe, B. S. Bauer, D. H. Dolan, J. R. Pillars, B. T. Hutsel, E. P. Yu, A. W. Klemmer, and S. E. Kreher, Phys. Plasmas **27**, 052705 (2020).

[75] C. E. Munroe, Am. J. Sci. **s3-36**, 48 (1888).

[76] W. Walters, *Fundamentals of Shaped Charges* (CMC Press, Baltimore, MD, 1998).

[77] J. J. MacFarlane, I. E. Golovkin, P. Wang, P. R. Woodruff, and N. A. Pereyra, High Energy Density Phys. **3**, 181 (2007).

[78] C. Kittel and H. Kroemer, *Thermal Physics, Second Edition* (W. H. Freeman & Company, New York, 1980), p. 276.

[79] F. Reif, *Fundamentals of Statistical and Thermal Physics* (McGraw–Hill, New York, 1965), p. 306.

[80] S. F. Garanin, S. D. Kuznetsov, W. L. Atchison, R. E. Reinovsky, T. J. Awe, B. S. Bauer, S. Fuelling, I. R. Lindemuth, and R. E. Siemon, IEEE Trans. Plasma Sci. **38**, 1815 (2010).

[81] S. F. Garanin, G. G. Ivanova, D. V. Karmishin, and V. N. Sofronov, J. Appl. Mech. Tech. Phys. **46**, 153 (2005).

[82] I. R. Lindemuth, R. E. Siemon, B. S. Bauer, M. A. Angelova, and W. L. Atchison, Phys. Rev. Lett. **105**, 195004 (2010).

[83] S. C. Bott-Suzuki, S. W. Cordaro, L. Atoyan, T. Byvank, W. Potter, B. R. Kusse, J. B. Greenly, D. A. Hammer, and C. A. Jennings, IEEE Trans. Plasma Sci. **46**, 1921 (2018).

[84] M. Bonitz, T. Dornheim, Zh. A. Moldabekov, S. Zhang, P. Hamann, H. Kählert, A. Filinov, K. Ramakrishna, and J. Vorberger, Phys. Plasmas **27**, 042710 (2020).

[85] *Frontiers and Challenges in Warm Dense Matter*, edited by F. Graziani, M. P. Desjarlais, R. Redmer, and S. B. Trickey (Springer, Berlin, 2014).

[86] T. M. Hutchinson, T. J. Awe, B. S. Bauer, B. T. Hutsel, D. A. Yager-Elorriaga, K. C. Yates, A. W. Klemmer, M. W Hatch, S. E. Kreher, E. P. Yu, and M. Gilmore, J. Appl. Phys. **130**, 153302 (2021).

[87] R. L. Masti, C. L. Ellison, W. A. Farmer, K. Tummel, and B. Srinivasan, Phys. Plasmas **28**, 102106 (2021).

[88] K. Tummel, D. R. Welch, D. V. Rose, A. J. Link, and K. R. LeChien, Phys. Plasmas **29**, 113102 (2022).

[89] N. Bennett, D. R. Welch, K. Cochrane, K. Leung, C. Thoma, M. E. Cuneo, and G. Frye-Mason, Phys. Rev. Accel. Beams **26**, 040401 (2023).

[90] R. L. Panton, *Incompressible Flow, Third Edition* (Wiley, New York, 2005).